Prospects for nuclear spin hyperpolarization of molecular samples using nitrogen-vacancy centers in diamond

J.-P. Tetienne,[1,2,*] L. T. Hall,[1] A. J. Healey,[1] G. A. L. White,[1] M.-A. Sani,[3] F. Separovic,[3] and L. C. L. Hollenberg[1,2,†]

[1]*School of Physics, University of Melbourne, Parkville, Victoria 3010, Australia*

[2]*Centre for Quantum Computation and Communication Technology, School of Physics, University of Melbourne, Parkville, Victoria 3010, Australia*

[3]*School of Chemistry, Bio21 Institute, University of Melbourne, Victoria 3010, Australia*

(Received 27 August 2020; revised 25 December 2020; accepted 5 January 2021; published 21 January 2021)

After initial proof-of-principle demonstrations, optically pumped nitrogen-vacancy (NV) centers in diamond have been proposed as a noninvasive platform to achieve hyperpolarization of nuclear spins in molecular samples over macroscopic volumes and enhance the sensitivity in nuclear magnetic resonance (NMR) experiments. In this work we model the process of polarization of external samples by NV centers and theoretically evaluate their performance in a range of scenarios. We find that average nuclear spin polarizations exceeding 10% can in principle be generated over macroscopic sample volumes ($\gtrsim\mu$l) with a careful engineering of the system's geometry to maximize the diamond-sample contact area. The fabrication requirements and other practical challenges are discussed. We then explore the possibility of exploiting local polarization enhancements in nano/micro-NMR experiments based on NV centers. For micro-NMR we find that modest signal enhancements over thermal polarization (by 1–2 orders of magnitude) can in essence be achieved with existing technology, with larger enhancements achievable via microstructuring of the sample/substrate interface. However, there is generally no benefit for nano-NMR where the detection of statistical polarization provides the largest signal-to-noise ratio. This work will guide future experimental efforts to integrate NV-based hyperpolarization to NMR systems.

DOI: 10.1103/PhysRevB.103.014434

I. INTRODUCTION

Nuclear magnetic resonance (NMR) is a powerful technique that can provide structural and dynamic information on molecular objects (NMR spectroscopy) and spatial information with submillimeter resolution for medical diagnosis and in materials science (NMR imaging, or MRI). The NMR signal generally originates from the weak thermal polarization (P_{th}) of nuclear spins at room temperature, for instance $P_{\text{th}} \approx 10^{-5}$ for protons in a magnetic field of 3 T. This constitutes a major limiting factor to the sensitivity of NMR spectroscopy [1], and consequently to the spatial resolution of MRI. A range of methods has been developed to enhance this polarization, denoted hyperpolarization methods, e.g., optical pumping [2,3], para-hydrogen-induced polarization (PHIP) [4,5], and dynamic nuclear polarization (DNP) [6–10]. In essence, all these methods rely on the creation of spin order in a given medium (a noble gas for optical pumping, a dihydrogen gas for PHIP, a solution containing unpaired electrons for DNP) and the subsequent transfer of this spin order to the nuclear spins of the target object. Using these techniques, polarizations (P_{HP}) far exceeding P_{th} are routinely achieved, typically from $P_{\text{HP}} \approx 5\%$ to 90%. However, they remain technically challenging to apply especially when the target molecules are in solution. For instance, PHIP involves the insertion of para-hydrogen into the target via catalytic hydrogenation, whereas DNP often relies on a freeze-thaw cycle where the polarization step takes place at cryogenic temperatures (typically below 20 K, or about 100 K for biological NMR applications [10]). Consequently, hyperpolarization techniques remain reserved for specialized applications.

Recently, the advent of solid-state spin systems originally developed for quantum information science has opened the prospect of a new avenue to achieve hyperpolarization. In particular, the nitrogen-vacancy (NV) center in diamond, whose electron spin can be rapidly ($\sim\mu$s) and efficiently polarized ($\approx$80%) at room temperature by optical pumping, has been proposed as an alternative source of spin order that could be transferred to the target molecules in a similar fashion to DNP [11–13]. Unlike conventional DNP, however, NV centers do not require cryogenic cooling or high magnetic fields, which could potentially enormously simplify the associated infrastructure. Moreover, diamond, being a chemically inert solid, can be relatively easily interfaced with the target molecules with minimum impact. But this also comes with a significant challenge: because the NV centers are relatively sparse and confined in a solid matrix (diamond) that is physically distinct from the target object, the contact area between the polarization source and the target is drastically reduced compared to standard hyperpolarization methods which involve a full mixing on molecular scales.

Proof-of-principle demonstrations of NV-based hyperpolarization were initially carried out on nuclear spins intrinsic to the diamond [14–25], and recently hyperpolarization of

*jtetienne@unimelb.edu.au
†lloydch@unimelb.edu.au

molecular spins external to the diamond was demonstrated with a single NV center via laboratory-frame cross relaxation (CR) [11] and nuclear spin orientation via electron spin locking (NOVEL) [12,13]. While the polarization in the immediate vicinity of the NV center can be quite high (≈80%) and scaling-up from these initial results appears encouraging [11], it remains unclear whether NV-based hyperpolarization is a viable approach to enhance NMR signals of macroscopic sample volumes.

In this work we address this question by modeling the general process of polarization of an ensemble of nuclear spins in contact with a diamond containing an ensemble of NV centers. We explore a range of scenarios and parameters and find that, even assuming an optimally efficient polarization transfer, obtaining large enhancements of the average nuclear polarization requires a careful structuring of the diamond in order to maximize the surface area in contact with the sample, which involves high-aspect-ratio microstructuring. Practical limitations such as finite NV spin coherence times or finite spin initialization fidelity, which place further constraints on this requirement, are discussed. We note that the theoretical framework we develop is general and in principle applicable to other solid-state systems hosting electron spins that can be polarized on demand.

Motivated by the fact that the polarization may be locally much higher than the average polarization, we then explore the possibility of enhancing the signal-to-noise ratio (SNR) in both NV-based micro-NMR and nano-NMR experiments, corresponding to sensing volumes of the order of $(10\ \mu\text{m})^3$ and $(10\ \text{nm})^3$, respectively [26–29]. For micro-NMR we find that modest enhancements over thermal polarization can be achieved under realistic assumptions, with current technology. For nano-NMR experiments, however, there is generally no SNR enhancement when compared with the standard detection of statistical polarization. Overall, these results highlight the limitations and challenges of NV-based hyperpolarization, and as such form the basis for developing a road map for future experimental efforts.

The paper is organized as follows. In Sec. II we present a theoretical framework to describe the polarization of an ensemble of nuclear spins using a single NV center. In Sec. III this framework is extended to the case of multiple NV centers arranged according to different geometries, and the resulting average polarization is compared to thermal polarization. This allows us to determine the influence of the different parameters and identify the requirements to achieve a significant polarization enhancement. In Sec. IV we analyze the case of NV-based micro- and nano-NMR. Finally, in Sec. V we conclude on the prospects on NV-based hyperpolarization and the experimental challenges ahead.

II. NV HYPERPOLARIZATION OF EXTERNAL TARGETS

In this paper we are interested in the problem of transferring spin polarization from sparse NV centers in a diamond structure to a comparatively dense ensemble of nuclear spins located outside the diamond (Fig. 1). This is a quite different situation to that encountered in conventional DNP experiments, and so we will start by discussing the key conceptual challenges for designing a "diamond hyperpolarizer"

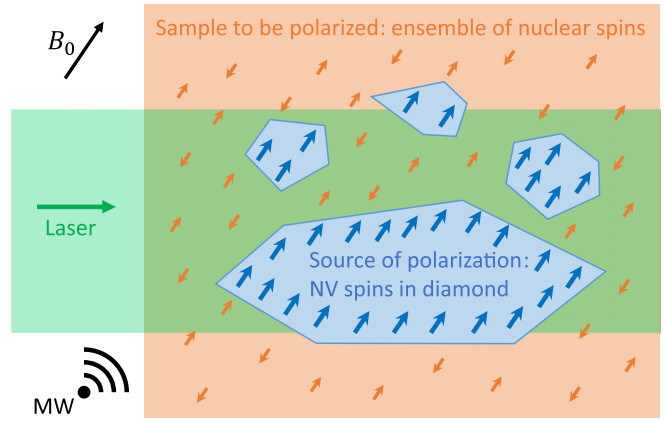

FIG. 1. Schematic illustrating the concept of NV-based hyperpolarization: diamond crystals (blue regions) containing NV spins (blue arrows) are in contact with a sample (orange region) containing nuclear spins (orange arrows). The NV spins are polarized by laser excitation and this polarization is transferred to the nuclear spins by microwave (MW) irradiation. The quantization axis is set by the external magnetic field, of strength B_0.

(Sec. II A). We will then describe the dynamics of polarization exchange between a single NV center and an ensemble of nuclear spins for a class of optimally efficient protocols (Sec. II B), and model the resulting build-up of polarization (Sec. II C). This model will be extended to the case of multiple NV centers arranged in certain specific geometries in Sec. III. We stress that although we consider the NV center as the source of polarization throughout this work, the results are quite general and could apply to any electron spin that can be initialized on demand, with only small corrections needed if the spin quantum number differs from the spin-1 NV system.

A. Conceptual challenges

The nature of the problem is illustrated in Fig. 1. Diamond crystals containing NV centers are brought in contact with a sample containing nuclear spins. The goal is to transfer the polarization from the optically pumped NV spins to the external nuclear spins. Compared to conventional DNP where the polarizing agents and the nuclear spins are mixed on the molecular scale, NV-based hyperpolarization faces two main hurdles.

The first hurdle is the physical separation between the sample and the NV spins, since the latter are confined inside diamond crystals. This means that there is a minimum distance of several nanometers between the sample and the NV spins closest to the diamond surface, and much more for deeper NVs, when conventional DNP typically involves separations of order ∼1 nm or less, consistent throughout the mixture. While the relative number of near-surface NVs can be maximized by choosing an appropriate geometry for the diamond structure, such as a stack of thin diamond plates or an assembly of spherical diamond nanoparticles (see Sec. III), the relatively large minimum gap remains a challenge. Nevertheless, because of their relative isolation the NV spins can have a relatively long lifetime ($T_{1,\text{NV}} \approx 5$ ms at room temperature [30]) and coherence time (approaching $T_{1,\text{NV}}$ with

dynamical decoupling [31]), and as a result polarization rates comparable to (or exceeding) those of conventional DNP may be achievable.

The second hurdle is that NV centers are typically sparse within a diamond crystal even with aggressive doping techniques [$\sim$10 ppm at most, i.e., roughly one NV per (10 nm)^3 volume, see discussion in Sec. III C 4]. This means there are very few NV centers available for each nuclear spin, especially if the diamond material occupies a small fraction of the total volume (diamond + sample), as discussed previously in Ref. [11]. For instance, for a sample containing 1 nuclear spin per (1 nm)^3 volume (i.e., a concentration of 1.7 M), there is a maximum of 1 NV per 10^3 nuclear spins assuming a 1:1 diamond/sample volume ratio (such as in a structure alternating diamond slabs and sample slabs of identical thickness), and 1 NV per $\sim 10^6$ nuclear spins if one uses diamond nanoparticles at a concentration of $\sim$1 g/l. In contrast, typical mixtures for DNP have 1 electron spin for just a few nuclear spins to be polarized.

Thus, NV hyperpolarization comes with a major disadvantage compared to conventional DNP, caused by the relatively low density and remote nature of the polarizing agents. The purpose of this work is to determine whether an efficient polarization transfer may be able to compensate for this deficit and make NV hyperpolarization competitive. To this end, we will initially consider an idealized scenario where the NV-nuclear system is perfectly coherent and polarization can be transferred at a rate simply limited by the strength of the magnetic dipole coupling. This is in contrast with conventional DNP where the mechanisms relied upon (e.g., solid effect, thermal mixing, Overhauser effect, etc. [6,7]) are designed to operate in a regime dominated by spin relaxation processes leading to transfer rates far below the dipolar coupling limit. Our aim is to use this best-case scenario to assess the potential of NV hyperpolarization and identify the main challenges and limiting factors. The effect of spin relaxation processes and other practical considerations will be discussed in Sec. III C.

B. Dynamics of polarization exchange

In this work we focus on a class of protocols that enable, in the absence of relaxation processes, coherent polarization transfer (flip-flop) between the NV spin and the target nuclear spin ensemble. This class includes CR [11], NOVEL [12–15], and the integrated solid effect [22], which rely on a continuous interaction, as well as pulsed protocols such as PulsePol [23], refocused NOVEL [24], and PolCPMG [25]. With the exception of CR which is microwave-free, all these protocols require microwave excitation resonant with the NV electron spin transition, and the flip-flop interaction is enabled by careful tuning of the microwave amplitude and/or pulsing parameters. Other protocols relying on thermal mixing, the cross effect or the solid effect, in conjunction with continuous repumping of the NV spin, were demonstrated [16–21], but they are designed to operate in a regime dominated by relaxation processes and thus are not considered here.

Let us consider the case of a single NV center interacting with a single nuclear spin located at a distance R, with a polar angle Θ relative to the quantization axis [Fig. 2(a)]. We assume that the NV center's electron spin (with gyromagnetic ratio γ_e) is perfectly initialized in the $|0\rangle$ state. The nuclear spin is a spin-$\frac{1}{2}$ with gyromagnetic ratio γ_n. We denote $p_\uparrow$ ($p_\downarrow$) as the probability for the nuclear spin to be in the $|\uparrow\rangle$ ($|\downarrow\rangle$) state. The spin polarization is then defined as $P = p_\uparrow - p_\downarrow$.

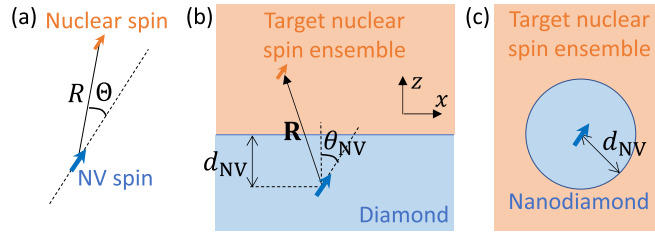

FIG. 2. Definitions of the geometrical parameters in the case of (a) a single NV spin (blue arrow) interacting with a single nuclear spin (orange arrow), (b) a single NV spin interacting with a semi-infinite slab of nuclear spins (orange box), and (c) a single NV spin at the center of a spherical nanodiamond (blue sphere) immersed in an infinite medium of nuclear spins. In (b), the orange arrow represents one spin among the ensemble, to define the position vector **R**.

For the class of coherent protocols mentioned above, the polarization P evolves as [11,32]

$$P(\tau) = P(0) + [1 - P(0)] \sin^2\left(\frac{A_s \tau}{2}\right), \tag{1}$$

where τ is the interaction time and A_s is the protocol-dependent flip-flop rate. Generally, CR offers the largest flip-flop rate followed by NOVEL and PulsePol, as shown in Ref. [32]. However, CR and NOVEL are not expected to operate in the coherent regime for external samples due to these protocols' sensitivity to surface-induced NV spin dephasing. Therefore, for all numerical evaluations, we will consider the PulsePol protocol as it is the most robust against dephasing and other imperfections [23] hence the best candidate to realize this idealized coherent scenario. Namely, for PulsePol the flip-flop rate is [23,32]

$$A_s = \frac{3\alpha a}{2R^3} |\sin(\Theta)\cos(\Theta)|, \tag{2}$$

where $a = \frac{\mu_0 \hbar \gamma_e \gamma_n}{4\pi}$ is the magnetic dipole coupling constant and $\alpha \approx 0.72$ is a numerical factor.

At time $\tau = \tau_0 \equiv \frac{\pi}{A_s}$, which we will refer to as the flip-flop time, the nuclear spin is fully polarized ($P = 1$) corresponding to a pure spin state $|\uparrow\rangle$. Thus, it takes a duration τ_0 to transfer a fraction [dependent on $P(0)$] of a single quantum of angular momentum from the NV spin to the nuclear spin. As an example, in this idealized scenario it would take $\tau_0 \approx 1.6$ ms to fully polarize a single proton spin (^{1}H) at a distance $R = 5$ nm and angle $\Theta = 54.7°$, using PulsePol. We note that the NV-^{1}H coupling strength (of order A_s) is much smaller than typical NV linewidths (kHz vs 100's of kHz), such that spin diffusion barrier effects can be safely neglected in what follows.

If the NV interacts with an ensemble of independent nuclear spins with uniform density ρ_n, it will still exchange polarization coherently with the ensemble but at a faster rate A_0 given by [11]

$$A_0^2 = \rho_n \int A_s^2(\mathbf{R}) d^3\mathbf{R}, \tag{3}$$

where $A_s(\mathbf{R})$ is the coupling strength for a spin located at position $\mathbf{R}$, which is given by Eq. (2) in the case of PulsePol. As before, the flip-flop time is defined as $\tau_0 \equiv \frac{\pi}{A_0}$.

The rate A_0 can be evaluated analytically for certain geometries. Let us first consider the case of a semi-infinite slab of nuclear spins placed on a flat diamond surface [Fig. 2(b)]. The NV center is located at a depth d_{NV} below the diamond surface and its spin quantization axis forms an angle θ_{NV} with the surface normal (defined as the z axis). In this case we obtain

$$A_0^2 = \frac{\rho_n (g\alpha a)^2}{d_{\mathrm{NV}}^3}, \tag{4}$$

where g is a dimensionless geometric factor given by

$$g^2 = \frac{\pi[55 + 12\cos(2\theta_{\mathrm{NV}}) - 3\cos(4\theta_{\mathrm{NV}})]}{1024}. \tag{5}$$

As an example, for ^{1}H spins in frozen water ($\rho_n = 66$ nm^{-3}) with $d_{\mathrm{NV}} = 5$ nm and $\theta_{\mathrm{NV}} = 54.7^\circ$ (yielding $g \approx 0.40$), we get a flip-flop time $\tau_0 \approx 30$ μs.

Alternatively, consider an NV center located at the center of a spherical diamond nanoparticle (nanodiamond) immersed in the nuclear spin ensemble [Fig. 2(c)]. If d_{NV} is the radius of the nanodiamond, A_0 takes the same form as in Eq. (4) but with a different geometric factor $g = \sqrt{\frac{2\pi}{5}} \approx 1.12$, which is nearly 3 times as large as for the flat surface. Accordingly, for ^{1}H in frozen water with $d_{\mathrm{NV}} = 5$ nm, the flip-flop time is shorter, $\tau_0 \approx 11$ μs.

From Eq. (4) it follows that the flip-flop time scales as $\tau_0 = \frac{\pi}{A_0} \propto d_{\mathrm{NV}}^{3/2} \rho_n^{-1/2} \gamma_n^{-1}$. A shallower NV will give a shorter flip-flop time, e.g., in the flat surface geometry $\tau_0 \approx 8$ μs for a 2-nm-deep NV, which is often considered a practical lower limit [33,34]. Meanwhile, more dilute samples will lead to longer times, e.g., $\tau_0 \approx 310$ μs for 1 M of ^{1}H spins in a deuterated solvent ($\rho_n = 0.6$ nm^{-3}, $d_{\mathrm{NV}} = 5$ nm), and 1 M of ^{13}C spins would give $\tau_0 \approx 1.2$ ms. These numbers illustrate the typical timescales involved in NV-based hyperpolarization.

It is important to note that the flip-flop time τ_0 corresponds to the transfer of a single (at most) quantum of angular momentum, provided by the NV spin. For an ensemble of nuclear spins, this transferred momentum must thus be shared among the nuclear spins, proportionally to their respective coupling strength. Precisely, the polarization of a nuclear spin at position $\mathbf{R}$, under a continuum approximation [11], evolves as

$$P(\mathbf{R}, \tau) = P(\mathbf{R}, 0) + [1 - P(\mathbf{R}, 0)] \frac{A_s^2(\mathbf{R})}{A_0^2} \sin^2\left(\frac{A_0 \tau}{2}\right). \tag{6}$$

To build up polarization, the NV therefore needs to be reinitialized and the protocol repeated, as we analyze below.

C. Modeling the polarization build-up

We consider the situation where the polarization transfer protocol is continuously repeated. That is, we continuously repeat a cycle consisting of initializing the NV spin to $|0\rangle$ and applying the protocol for a duration τ. Each cycle increases the polarization by a small amount, as described by Eq. (6). The polarization after each cycle of duration τ, which we denote as $P(\mathbf{R}, t)$ where t is the total time (a multiple of τ), can then be described by a differential equation $\frac{\partial P}{\partial t} = u(1 - P)$ where u is the position-dependent polarization rate, or "cooling" rate, given by

$$\begin{aligned} u(\mathbf{R}) &= \frac{P(\mathbf{R}, t + \tau) - P(\mathbf{R}, t)}{\tau[1 - P(\mathbf{R}, t)]} \\ &= \frac{1}{\tau} \frac{A_s^2(\mathbf{R})}{A_0^2} \sin^2\left(\frac{A_0 \tau}{2}\right). \end{aligned} \tag{7}$$

The optimum duration τ to maximize $u(\mathbf{R})$ is $\tau_{\mathrm{opt}} \approx 0.74\tau_0$ and gives $u(\mathbf{R}) \approx \frac{1.14}{\tau_0} \frac{A_s^2(\mathbf{R})}{A_0^2}$. The differential equation produced can be extended to include spin-lattice relaxation of the nuclear spins (relaxation rate $\Gamma_{1,n}$) as well as polarization diffusion (diffusion coefficient D_n), leading to the differential equation [11]

$$\begin{aligned} \frac{\partial P(\mathbf{R}, t)}{\partial t} &= u(\mathbf{R})[1 - P(\mathbf{R}, t)] \\ &\quad - \Gamma_{1,n} P(\mathbf{R}, t) + D_n \nabla^2 P(\mathbf{R}, t). \end{aligned} \tag{8}$$

The diffusion term may capture molecular diffusion in the case of a liquid sample (assuming diffusion is slow enough that the flip-flop dynamics described in the previous section remains approximately valid, see Sec. III C 3), or dipole-mediated spin diffusion in the case of a solid sample.

Before solving Eq. (8) numerically in the general case, it is useful to examine the solution when diffusion is neglected ($D_n = 0$),

$$P(\mathbf{R}, t) = P(\mathbf{R}, \infty)[1 - e^{-[u(\mathbf{R}) + \Gamma_{1,n}]t}], \tag{9}$$

where we assumed that the sample is initially unpolarized, $P(\mathbf{R}, 0) = 0$, and the steady-state value is given by

$$P(\mathbf{R}, \infty) = \frac{u(\mathbf{R})}{u(\mathbf{R}) + \Gamma_{1,n}}. \tag{10}$$

This steady-state value is reached in a time of the order of the relaxation time $T_{1,n} = 1/\Gamma_{1,n}$, or less if $u(\mathbf{R}) \gg \Gamma_{1,n}$. As an example, for ^{1}H spins in a dense ensemble ($\rho_n = 66$ nm^{-3}) with $d_{\mathrm{NV}} = 5$ nm and $\theta_{\mathrm{NV}} = 54.7^\circ$, $u(\mathbf{R})$ reaches up to $\approx$15 s^{-1} at some positions $\mathbf{R}$, leading to a maximum steady-state polarization of $\approx$94% if $T_{1,n} = 1$ s. Cross sections of the polarization distribution for this scenario are shown in Fig. 3(a), revealing a multilobe structure originating from the angular dependence of the dipolar interaction [Eq. (2)].

Diffusion acts to spread the polarization further away from the source (i.e., the NV), but the timescale to reach the steady state remains relatively unchanged, constrained by $T_{1,n}$. Using the approximate expression for a cubic lattice, $D_n \approx 0.22 \frac{\mu_0}{4\pi} \hbar \gamma_n^2 \rho_n^{1/3}$ [35], we obtain $D_n \approx 670$ nm^2 s^{-1} under the same assumptions as before. The spatial extent of the polarization is thus expected to be of the order of $\sqrt{D_n T_{1,n}} \approx 30$ nm. Polarization maps for this scenario are shown in Fig. 3(b) where the polarization indeed extends over 10's of nanometers, much further than without diffusion, while the maximum polarization is reduced to <4% [note that Fig. 3(b) was cropped to show the same region as Fig. 3(a) but the polarization extends beyond this region].

A figure of merit to quantify the efficiency of the polarization process is the effective number of polarized spins, defined

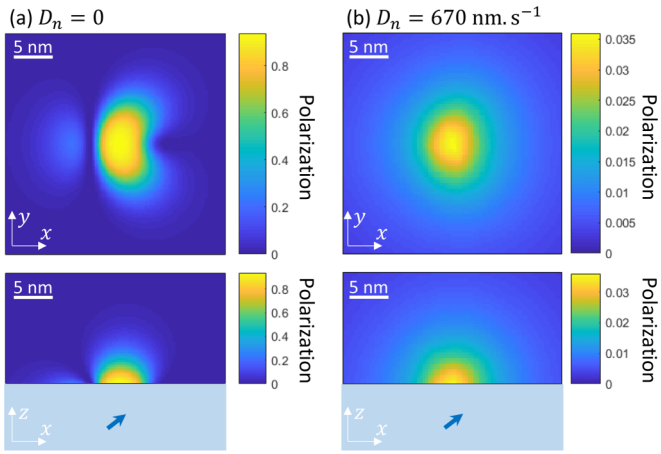

FIG. 3. Calculated polarization maps in the steady state $[P(\mathbf{R}, \infty)]$ in the xy plane at the diamond-sample interface (top) and in the xz plane encompassing the NV (bottom) without diffusion (a) and with $D_n = 670$ nm^2 s^{-1} (b). The NV spin has a depth $d_{\mathrm{NV}} = 5$ nm and is oriented at an angle $\theta_{\mathrm{NV}} = 54.7°$ in the xz plane. The nuclear spins (^{1}H) have a density $\rho_n = 66$ nm^{-3} and a relaxation time $T_{1,n} = 1$ s. The PulsePol protocol is applied with an interaction time $\tau = \tau_{\mathrm{opt}} = 22\ \mu$s.

as

$$N_{\mathrm{s}} = \rho_n \int P(\mathbf{R}, \infty) d^3\mathbf{R}. \tag{11}$$

In the conditions of Fig. 3 we obtain $N_{\mathrm{s}} \approx 20\,000$ without diffusion, and $N_{\mathrm{s}} \approx 37\,000$ with $D_n = 670$ nm^2 s^{-1}. The difference is due to a saturation effect: as P approaches 1, the rate of change $\frac{\partial P}{\partial t}$ decreases [see Eq. (8)]; therefore, by keeping the local polarization to a low level, diffusion allows for a higher total polarization to be reached.

The effect of diffusion is further illustrated in Fig. 4(a) which plots N_{s} with and without diffusion, as a function of $T_{1,n}$. For $T_{1,n} \lesssim 0.1$ s, diffusion has little effect on N_{s} because the polarization levels remain $\ll 1$, but for larger $T_{1,n}$ we see that N_{s} becomes comparatively smaller without diffusion due to this saturation effect. Meanwhile, with diffusion N_{s} grows

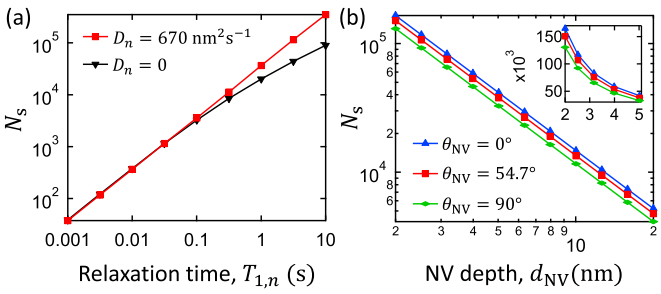

FIG. 4. (a) Calculated effective number of polarized spins in the steady state N_{s} as a function of $T_{1,n}$ for ^{1}H spins with $\rho_n = 66$ nm^{-3} and $D_n = 670$ nm^2 s^{-1} (red data) or $D_n = 0$ (black). The NV spin is such that $d_{\mathrm{NV}} = 5$ nm and $\theta_{\mathrm{NV}} = 54.7°$. (b) N_{s} as a function of d_{NV} for ^{1}H spins with $\rho_n = 66$ nm^{-3}, $D_n = 670$ nm^2 s^{-1}, and $T_{1,n} = 1$ s. The NV angle is $\theta_{\mathrm{NV}} = 0°$ (blue data), 54.7° (red), and 90° (green). The inset is a zoom in the shallow region ($d_{\mathrm{NV}} \leqslant 5$ nm) plotted against linear scales to facilitate reading.

linearly with $T_{1,n}$, as anticipated from Eq. (10) which gives $P(\mathbf{R}, \infty) \approx u(\mathbf{R}) T_{1,n}$ in the limit $u(\mathbf{R}) \ll \Gamma_{1,n}$ (i.e., far from saturation). In this limit, evaluating Eq. (11) using the expression for $u(\mathbf{R})$ from Eq. (7) gives

$$N_{\mathrm{s}} \approx 1.14 \frac{T_{1,n}}{\tau_0}, \tag{12}$$

where we chose the optimal time $\tau = \tau_{\mathrm{opt}}$. Thus, we find, quite as expected, that the number of polarized spins is roughly the maximum build-up time ($\sim T_{1,n}$) divided by the time it takes to polarize one spin (τ_0). Evaluating τ_0 using Eq. (4) we obtain

$$N_{\mathrm{s}} \approx g' a T_{1,n} \rho_n^{1/2} d_{\mathrm{NV}}^{-3/2} \tag{13}$$

$$\propto \gamma_n T_{1,n} \rho_n^{1/2} d_{\mathrm{NV}}^{-3/2}, \tag{14}$$

where we defined an extended geometric factor $g' = 1.14 \alpha g/\pi$ that incorporates the numerical factors (note that α depends on the protocol, $\alpha \approx 0.72$ for PulsePol).

For the flat surface geometry [Fig. 2(b)], g depends on the NV angle θ_{NV} [see Eq. (5)]. This dependence is illustrated in Fig. 4(b) which plots N_{s} as a function of the NV depth d_{NV} varying from 2 to 20 nm, for different angles θ_{NV}. We see that a maximum polarization is achieved with $\theta_{\mathrm{NV}} = 0°$ corresponding to the NV axis along z (blue data), followed by $\theta_{\mathrm{NV}} = 54.7°$ and $\theta_{\mathrm{NV}} = 90°$ which are about 10% and 30% less efficient, respectively. Nevertheless, these differences are small compared to the effect of d_{NV}, as expected from the $N_{\mathrm{s}} \propto d_{\mathrm{NV}}^{-3/2}$ scaling. In the following we will assume $\theta_{\mathrm{NV}} = 54.7°$, which is the most commonly found angle as it corresponds to a (100)-oriented diamond surface.

III. NV-BASED HYPERPOLARIZATION FOR CONVENTIONAL NMR

In the previous section we developed a framework to predict the maximum number of spins that can be polarized by a single NV spin N_{s} [Eq. (13)]. Here we analyze how macroscopic ensembles of NV centers can be arranged to produce a sizable polarization over a sample volume compatible with conventional NMR ($\sim\mu$l to ml). We analyze two different architectures for such a diamond hyperpolarizer, and for each we determine the requirements to achieve a polarization enhancement.

A. Slab architecture

We first consider the geometry proposed in Ref. [11] and depicted in Fig. 5(a), which employs a stack of diamond slabs comprising arrays of near-surface NV centers on each side, with an areal density σ_{NV}. The NVs are located at a depth d_{NV} from the diamond surface and form an angle θ_{NV} with the z axis (normal to the diamond surface). The gap between diamond slabs, filled with the sample to be polarized, is h_{cell}. The unit cell of this structure is therefore a slab of sample of thickness $h_{\mathrm{cell}}/2$, polarized by a single layer of NV spins. If N_{s} is the number of polarized spins due to a single NV spin within the array, the polarization will be, when averaged over

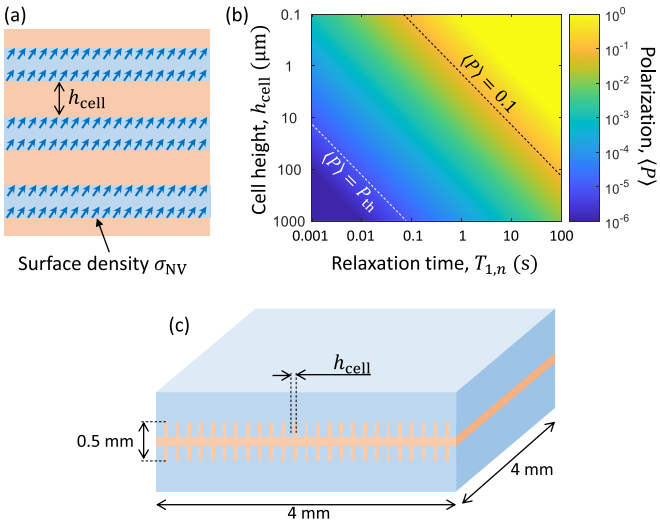

FIG. 5. (a) A slab architecture for the hyperpolarization of a macroscopic sample (orange regions) based on a stack of diamond slabs (blue) with near-surface NV centers (blue arrows) on both sides. (b) Average polarization induced by the NVs $\langle P\rangle$ as a function of $T_{1,n}$ and h_{cell}, in the geometry (a) for ^{1}H spins. The other parameters are: $\sigma_{NV} = 10^{16}$ m^{-2}, $d_{NV} = 5$ nm, $\rho_n = 0.6$ nm^{-3}. The white (black) dashed line indicates $\langle P\rangle = P_{th}$ ($\langle P\rangle = 0.1$). $\langle P\rangle$ is calculated using Eq. (15), which assumes that the polarization is $\ll 1$ at any point in the sample. Thus, the plot is not meant to be accurate in the region where $\langle P\rangle$ approaches unity. Where Eq. (15) predicts $\langle P\rangle > 1$, the value was capped to 1. (c) Example of a diamond hyperpolarizer based on the geometry (a). Two diamond plates are structured to feature h_{cell}-wide grooves and sealed together. Example dimensions are indicated, yielding a total sample volume of ≈5 μl.

the entire sample,

$$\langle P\rangle = \frac{2\sigma_{NV}N_s}{\rho_n h_{cell}} \tag{15}$$

$$= \frac{2\sigma_{NV}g' a T_{1,n}}{\rho_n^{1/2} d_{NV}^{3/2} h_{cell}}, \tag{16}$$

where the second line used Eq. (13), g' being the geometric factor for the slab geometry ($g' \approx 0.11$ for $\theta_{NV} = 54.7°$).

We compare this NV-induced polarization with the thermal polarization [1],

$$P_{th} = \tanh\left(\frac{\hbar\gamma_n B_0}{2k_B T}\right), \tag{17}$$

where B_0 is the magnetic field, T is the temperature, and k_B is the Boltzmann constant. In the following we will compare $\langle P\rangle$ to the thermal polarization obtained at $B_0 = 3$ T and $T = 300$ K, i.e., $P_{th} \approx 10^{-5}$ for ^{1}H spins. The 3 T value was chosen to be representative of conventional NMR/MRI experiments, keeping in mind that P_{th} scales approximately as $P_{th} \propto B_0$ so that a 9 T NMR spectrometer, for example, would give a polarization 3 times as large as that assumed here. We note that P_{th} and $\langle P\rangle$ (via the constant a) are both proportional to the gyromagnetic ratio γ_n, therefore the ratio $\langle P\rangle/P_{th}$ is independent of the nucleus considered.

Let us examine how the parameters in Eq. (16) can be optimized to achieve $\langle P\rangle \gg P_{th}$. The NV density σ_{NV} must be maximized, but is limited by material considerations to maximum values of the order of $\sigma_{NV} \sim 10^{16}$ m^{-2} (see discussion in Sec. III C 4). The NV depth d_{NV} must be minimized but is also limited to a minimum of a few nanometers typically. The density ρ_n depends on the sample to be polarized but has a relatively weak effect ($\rho_n^{1/2}$ scaling) compared to other parameters. The remaining parameters are $T_{1,n}$, which can vary over several orders of magnitude depending on the sample, and h_{cell} which depends on the engineering of the system and could vary from mm to μm scales. To explore the parameter space, we therefore vary $T_{1,n}$ and h_{cell} while fixing the other parameters to nominal typical values: $\sigma_{NV} = 10^{16}$ m^{-2}, $d_{NV} = 5$ nm, $\rho_n = 0.6$ nm^{-3} (i.e., 1 M).

The outcome of this parameter sweep is presented in Fig. 5(b). The white dashed line corresponds to the $\langle P\rangle = P_{th}$ condition, implying that there is no polarization enhancement below this line, whereas the black dashed line indicates a large enhancement, $\langle P\rangle = 0.1 \approx 10^4 P_{th}$. With $h_{cell} = 100$ μm, we obtain a modest enhancement $\langle P\rangle \approx 100 P_{th}$ with $T_{1,n} = 1$ s, which is a typical relaxation time for ^{1}H. The polarization is increased to ≈10% if $T_{1,n} = 100$ s, which is relevant to low-γ_n nuclei (e.g., ^{15}N or ^{13}C) and also relevant for low temperatures. A 10% polarization could be obtained for $T_{1,n} = 1$ s if the gap is reduced to $h_{cell} \approx 1$ μm.

An example structure facilitating the implementation of this architecture is depicted in Fig. 5(c). It is composed of two diamond plates structured with h_{cell}-wide grooves. With 4×4 mm^2 overall lateral dimensions, which corresponds to standard commercially available diamond plates, the sample volume enclosed by this structure would be ≈5 μl if the grooves are ≈200 μm deep. While this volume remains smaller than the capacity of standard NMR probes (100's of μl), it is already comparable to the capacity of some NMR microprobes and could be increased with deeper grooves, larger diamond plates, or by repeating the building block of Fig. 5(c).

Based on this structure, $h_{cell} = 100$ μm would be relatively straightforward to realize with standard etching techniques given the aspect ratio close to unity. However, $h_{cell} = 1$ μm (aspect ratio ∼100) is a much more challenging target that will require further experimental developments. Diamond gratings with aspect ratios of 10–20 are routinely fabricated for optical components [36–38], and diamond needles with aspect ratios up to 50 have also been reported [39,40]. We stress that the above requirements correspond to an idealized scenario where the polarization transfer from NV to sample is optimally efficient. In Sec. III C we will discuss practical limitations to this polarization transfer efficiency, and how these may impose stronger requirements, e.g., a smaller h_{cell}.

We note that hyperpolarization may add a temporal overhead to the overall NMR acquisition procedure, such that the enhancement of the SNR is reduced compared to the $\langle P\rangle/P_{th}$ ratio [1]. This would be the case, for instance, of liquid-state NMR requiring a freeze-thaw process to incorporate the hyperpolarization step, as will be discussed in Sec. III C 3. However, for solid-state NMR when the hyperpolarization protocol is applied continuously, the SNR enhancement is essentially given by the polarization enhancement $\langle P\rangle/P_{th}$.

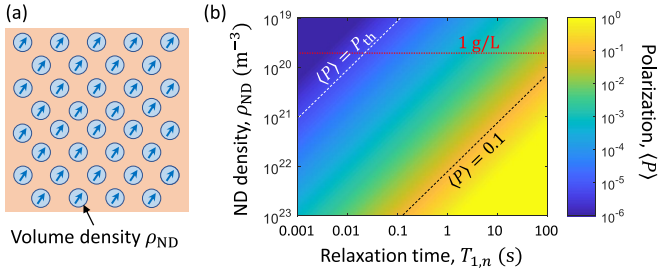

FIG. 6. (a) A nanodiamond architecture for the hyperpolarization of a macroscopic sample (orange region) based on an assembly of spherical nanodiamonds (blue spheres) with a single NV (blue arrows) per nanodiamond. (b) Average polarization induced by the NVs $\langle P\rangle$ as a function of $T_{1,n}$ and ρ_{ND}, in the geometry (a) for ^{1}H spins. The other parameters are: $d_{NV} = 10$ nm, $\rho_n = 0.6$ nm^{-3}. The white (black) dashed line indicates $\langle P\rangle = P_{th}$ ($\langle P\rangle = 0.1$). $\langle P\rangle$ is calculated using Eq. (18), which assumes that the polarization is $\ll 1$ at any point in the sample. Thus, the plot is not meant to be accurate in the region where $\langle P\rangle$ approaches unity. Where Eq. (18) predicts $\langle P\rangle > 1$, the value was capped to 1. The red dotted line indicates an equivalent nanodiamond concentration of 1 g/l.

B. Nanodiamond architecture

We next consider the use of spherical nanodiamonds immersed in the sample, with a uniform volume density ρ_{ND} [Fig. 6(a)]. We take a nanodiamond radius of $d_{NV} = 10$ nm, since below this radius NV centers are typically not charge stable on average [41], although we note that taking $d_{NV} = 5$ nm as previously would lead to similar conclusions due to the relatively slow scaling [$N_s \propto d_{NV}^{-3/2}$, see Eq. (13)]. We assume that each nanodiamond contains a single NV center, corresponding to an NV concentration of a few ppm. For simplicity the NV is assumed to be located at the center of the sphere, with its axis aligned with the external magnetic field. If N_s is the number of polarized spins due to a single nanodiamond, the polarization of the sample will be, on average,

$$\langle P\rangle = \frac{\rho_{ND} N_s}{\rho_n} \tag{18}$$

$$= \frac{\rho_{ND} g' a T_{1,n}}{\rho_n^{1/2} d_{NV}^{3/2}}, \tag{19}$$

where the geometric factor is $g' \approx 0.29$.

Figure 6(b) plots $\langle P\rangle$ as a function of $T_{1,n}$ and ρ_{ND} for ^{1}H spins with a density $\rho_n = 0.6$ nm^{-3} (1 M). For $T_{1,n} \approx 1$ s, a 10% polarization would require $\rho_{ND} \approx 10^{22}$ m^{-3}, corresponding to a nanodiamond concentration of ≈150 g/l or a ≈4% volume/volume concentration. Such a concentration is two orders of magnitude larger than that of commercially available colloidal solutions (typically ∼1 g/l [42]) and would be difficult to reach in a liquid environment while maintaining an even dispersion, but could potentially be achieved in a solid mixture. However, nanodiamonds suffer from significant drawbacks such as a reduced NV charge stability and reduced spin coherence due to the increased surface-to-volume ratio [41,43], and the random NV orientation implying that only a small fraction of the nanodiamonds would in fact contribute to the polarization. In Ref. [23] a fraction of active nanodiamonds of about 10% was estimated, making the density requirements even more stringent if not physically impossible, e.g., a 40% volume/volume nanodiamond concentration would be required to achieve a 10% polarization, under the same assumptions as above. For these reasons, the discussions that follow will focus on the slab geometry that appears more promising, although they largely apply to nanodiamonds as well.

C. Practical considerations

In this section we discuss practical aspects of NV experiments relevant to the implementation of hyperpolarization. First, we will see how the polarization transfer rate is affected by imperfect NV initialization, finite NV coherence time, and fast molecular diffusion within the sample. Next, we will discuss the practical limits to increasing the NV density, the effect of parasitic spins, and the requirements associated with laser illumination and background magnetic field.

1. NV initialization

In Sec. II B we assumed that the NV electron spin can be perfectly and instantly initialized into a pure spin state. In reality, the NV initialization fidelity is finite, $\mathcal{F}_{NV} < 1$. A typical observed value is $\mathcal{F}_{NV} \approx 0.8$ for single NV centers in a bulk diamond [44], but $\mathcal{F}_{NV}$ may be lower for near-surface NV centers, which are often subject to additional ionization dynamics [45,46]. Existing strategies to improve this fidelity generally involve significant time overheads and so are not considered here. The factor $\mathcal{F}_{NV}$ can be simply included in the cooling rate $u(\mathbf{R})$ as a multiplying factor [Eq. (7)].

Furthermore, initialization of the NV electron spin is not instantaneous. It typically takes a minimum of 1 μs of optical pumping under high laser intensity, followed by 1 μs to allow the NV to relax to its ground state [47], before the polarization transfer protocol can be applied. This can be taken into account in our model by adding a dead time $t_d \geqslant 2$ μs to τ in the denominator of Eq. (7). At lower laser intensity, as often required when addressing large volumes of NV centers (see Sec. III C 6), this dead time may be as large as 10's of μs, which could reduce $u(\mathbf{R})$ if the flip-flop time τ_0 is comparable.

2. NV dephasing

The NV spin typically experiences some dephasing even in the absence of the sample. Protocols such as PulsePol are, by design, robust against quasistatic dephasing, but faster fluctuations will still contribute to reduce the efficiency of the polarization transfer. As a crude approximation, this can be taken into account by including a damping factor $e^{-\tau/T_{2,NV}}$ in the expression of $u(\mathbf{R})$, where $T_{2,NV}$ is the coherence time of the NV electron spin under the PulsePol sequence (a rigorous treatment of dephasing effects is presented in Ref. [32]). For an NV at a depth $d_{NV} = 5$ nm, $T_{2,NV}$ can be as large as ∼1 ms with optimized diamond surface preparation and low density of NV centers [48]. However, values in the range $T_{2,NV} \sim 10$–100 μs are more commonly observed in samples with large densities of near-surface NVs [49]. This is much shorter than the optimum interaction time expected for low-γ_n

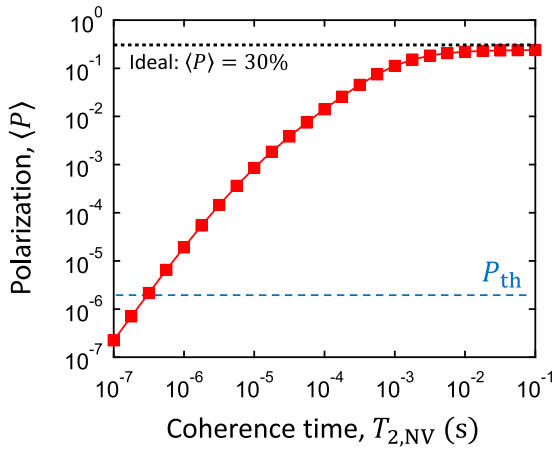

FIG. 7. Average polarization induced by the NVs $\langle P\rangle$ as a function of the NV spin coherence time $T_{2,\mathrm{NV}}$. $\langle P\rangle$ is calculated for 1 M of ^{13}C spins in the geometry of Fig. 5(a) with $h_{\mathrm{cell}} = 10\ \mu$m. For each value of $T_{2,\mathrm{NV}}$, the optimum cooling rate from Eq. (20) is used. The other parameters are: $T_{1,n} = 100$ s, $d_{\mathrm{NV}} = 5$ nm, $\theta_{\mathrm{NV}} = 54.7°$, $\mathcal{F}_{\mathrm{NV}} = 0.8$, $t_d = 10\ \mu$s, $\sigma_{\mathrm{NV}} = 10^{16}$ m^{-2}. The black dotted line corresponds to the ideal case where $\mathcal{F}_{\mathrm{NV}} = 1$, $t_d = 0$, and $T_{2,\mathrm{NV}} = \infty$. The blue dashed line indicates the thermal polarization $P_{\mathrm{th}} \approx 2.6 \times 10^{-6}$ assuming $B_0 = 3$ T and $T = 300$ K.

nuclei, e.g., $\tau_0 \approx 1.2$ ms for 1 M of ^{13}C spins, which will significantly reduce the cooling rate.

Combining the above factors, we can rewrite the cooling rate as

$$u(\mathbf{R}) = \frac{\mathcal{F}_{\mathrm{NV}} e^{-\frac{\tau}{T_{2,\mathrm{NV}}}}}{\tau + t_d} \frac{A_s^2(\mathbf{R})}{A_0^2} \sin^2\left(\frac{A_0\tau}{2}\right). \tag{20}$$

The optimum interaction $\tau = \tau_{\mathrm{opt}}$ maximizing $u(\mathbf{R})$ now depends not only on A_0 but also on t_d and $T_{2,\mathrm{NV}}$. The effect of these factors is illustrated in Fig. 7, which plots the average polarization ($\langle P\rangle$) of 1 M of ^{13}C spins in the geometry of Fig. 5(a), as a function of $T_{2,\mathrm{NV}}$ assuming $\mathcal{F}_{\mathrm{NV}} = 0.8$ and $t_d = 10\ \mu$s (red line). Compared to the ideal case (horizontal dotted line), $\langle P\rangle$ is reduced from 30% to 24% for $T_{2,\mathrm{NV}} \gtrsim 10$ ms, and drops to 1.4% for $T_{2,\mathrm{NV}} = 100\ \mu$s and <0.1% for $T_{2,\mathrm{NV}} = 10\ \mu$s. Even though these polarization levels still largely exceed the thermal polarization, it is clear that the finite NV coherence time is an important limiting factor for NV hyperpolarization. This motivates further work on improving spin coherence of shallow NV centers [48], which in principle can approach the phonon limit of, e.g., $T_{2,\mathrm{NV}} \sim 1$ s at 77 K [31], as well as exploring other protocols that may be more efficient in the $T_{2,\mathrm{NV}}$-limited regime [32].

3. Molecular diffusion

Most conventional DNP methods are inefficient in the presence of fast molecular diffusion, except for the Overhauser effect in some conditions [50]. For NV centers located several nanometers from the surface, however, the interaction correlation time is too long for the Overhauser effect to work effectively [51], but is still too short for other methods including the coherent polarization exchange scenario considered in Sec. II B.

To see that, consider the example of liquid water at room temperature, which has a diffusion coefficient of $D_n \approx 2.5 \times 10^{-9}$ m^2 s^{-1}. Over the timescale of the flip-flop dynamics ($\tau_0 \approx 30\ \mu$s), the ^{1}H spins travel over typical distances $\sim\sqrt{D_n\tau_0} \sim 300$ nm. This is much larger than the distance over which the NV-nuclear coupling is significant (of the order of d_{NV}). In the framework of Sec. II B it is as if the state of the nuclear spins was being reset to an unpolarized, incoherent mixture every $t_D \sim d_{\mathrm{NV}}^2/D_n = 10$ ns for $d_{\mathrm{NV}} = 5$ nm. This leads to a Zeno-type effect whereby the NV spin, instead of exchanging polarization following a $\sin^2\left(\frac{A_0\tau}{2}\right)$ law, would supply an amount $[\sin^2\left(\frac{A_0 t_D}{2}\right)]^{\frac{\tau}{t_D}} \approx \left(\frac{A_0 t_D}{2}\right)^{\frac{2\tau}{t_D}}$, which becomes rapidly negligible for $t_D \ll \tau_0$.

Thus, the results presented in the previous sections are valid only for solid samples or high-viscosity liquid samples, typically $D_n \lesssim 10^{-14}$ m^2 s^{-1}. Nevertheless, liquid samples such as aqueous solutions could be handled in a similar fashion to conventional dissolution DNP, where the solution is frozen for the hyperpolarization step and thawed for the NMR measurement [52–54]. Here the solution would simply need to be cooled below the freezing point, in contrast to DNP where a much lower temperature is required to achieve high polarization.

4. NV density

In Sec. III A we introduced a surface density of NV centers σ_{NV} which should be maximized to increase the average polarization, according to Eq. (15). Here we discuss the practical limits to increasing σ_{NV}.

Dense ensembles of near-surface NV centers are typically produced by nitrogen (N) ion implantation [49]. For a fluence of 10^{13} N/cm^2, assuming a 4% N-to-NV conversion efficiency and taking into account that only 25% of the NV centers will have the correct crystallographic orientation and be aligned with the applied magnetic field [55], the surface density of "active" NVs is $\sigma_{\mathrm{NV}} = 10^{15}$ m^{-2}. Obtaining larger surface densities with this method is challenging especially at the low implantation energies required to create shallow NV centers, e.g., 2.5 keV to obtain a depth $d_{\mathrm{NV}} \approx 5$ nm. Indeed, a 2.5 keV implant with a 10^{13} N/cm^2 fluence already creates locally about 100 ppm of N, and 2000 ppm of vacancies before annealing, according to stopping and range of ions in matter (SRIM) Monte Carlo simulations. Significantly larger fluences would likely cause irreparable damage and significantly reduce the spin coherence time $T_{2,\mathrm{NV}}$ (limited by the bath of surrounding paramagnetic impurities). It might be possible to increase the NV density without increasing the fluence, through doping engineering to improve the N-to-NV yield [56–58], but further work is needed to test the efficiency of this approach for dense layers of shallow NVs.

However, for applications where the NVs are not used for readout as in Sec. III A, the NVs do not need to be restricted to the near-surface region, which opens the possibility to use optimized bulk doping techniques. In particular, a record high bulk NV density of 45 ppm was achieved in Ref. [59], through electron irradiation and *in situ* annealing of a diamond naturally containing about 100 ppm of nitrogen. Counting only those 25% of the NVs that would be aligned with the external

magnetic field, i.e., ≈11 ppm of active NVs, a 5-nm slice in this diamond would give a surface density $\sigma_{\mathrm{NV}} \approx 10^{16}$ m^{-2}. In Sec. III A we assumed $\sigma_{\mathrm{NV}} = 10^{16}$ m^{-2} with a fixed depth $d_{\mathrm{NV}} = 5$ nm, which is therefore a good approximation for this diamond.

It is important to note that the NV density directly competes with the NV coherence time $T_{2,\mathrm{NV}}$. For instance, when substitutional nitrogen (N) is the dominant impurity, the NV coherence time is inversely proportional to the density [N] [60]. Since the NV density is proportional to [N], assuming a constant conversion efficiency, increasing the NV density therefore does not necessarily result in an increased polarization. Dynamical decoupling experiments performed on diamonds with [N] ∼100 ppm reported coherence times of up to $T_{2,\mathrm{NV}} \sim 100$ μs [61]. This is sufficient not to limit the cooling rate in the case of a dense ^{1}H ensemble, but is already a limiting factor for more dilute samples (see Fig. 7). Thus, the assumed density of $\sigma_{\mathrm{NV}} = 10^{16}$ m^{-2} can be considered an optimum trade-off with respect to $T_{2,\mathrm{NV}}$.

We note that a surface density $\sigma_{\mathrm{NV}} = 10^{16}$ m^{-2} corresponds to a typical lateral distance between NVs of ≈10 nm. Given that the polarization exchange dynamics between NV and nuclear spins is dominated by the most strongly coupled nuclear spins at a distance $\sim d - 2d$, the presence of nearby NV centers in the array may affect this dynamics slightly, and as a result change the number of polarized spins per NV, N_{s}. For simplicity, this potential correction was neglected in Sec. III A.

5. Parasitic spins

In addition to the NV spins, the diamond hosts a number of parasitic spins that may contribute to reducing the amount of polarization reaching the target sample, via two different mechanisms. First, unpaired electron spins from defects located inside the diamond (such as nitrogen impurities or vacancy clusters [49]) or on the diamond surface [62–65] act as a source of dephasing for the nuclear spins in the sample, which could affect the dynamics of the NV-sample system during the polarization transfer and therefore the efficiency of the process [32].

Second, the diamond hosts nuclear spins (inside or at the surface) that could act as competing polarization sinks reducing the amount of polarization transferred to the target sample. Inside the diamond, ^{14}N and/or ^{15}N spins are typically present, as well as ^{13}C spins if the diamond is not isotopically purified. Moreover, an adventitious layer of ^{1}H spins of thickness 1–2 nm (density $\rho_n \sim 50$ nm^{-3}) is often observed on the diamond surface [66,67].

6. Laser illumination

An important element of NV experiments is the laser illumination at 532 nm wavelength (or similar), which enables the initialization of the NV spin to a nearly pure state, as discussed in Sec. III C 1. The illumination time required to fully initialize the NV spin depends on the laser intensity, with ∼100 kW/cm^2 typically employed to initialize the NV in ∼1 μs [47]. To initialize a 1 mm^2 array of NVs at normal incidence, a peak laser power of 1 kW would be required to achieve this initialization time, highlighting the enormous challenge posed by laser illumination in mm-sized devices such as the structure presented in Fig. 5(c). While lower laser intensities may be used, this comes at the cost of a reduced polarization rate (see Sec. III C 1). Careful optical engineering exploiting, e.g., waveguiding and multipass strategies [68], will therefore be critical for this application.

A deleterious consequence of laser illumination is the heating or photodamage it may induce on the sample to be polarized. Laser-induced heating is particularly problematic when the sample must be frozen to allow polarization. Critically, the desired close proximity between NV and sample ($d_{\mathrm{NV}} \sim 5$ nm) means that the laser intensity in the sample (near the diamond surface) will be similar to that in the NV layer regardless of the illumination configuration, and precludes the use of laser shielding. However, we note that laser heating, if it can be tuned appropriately, could also be used as a resource to thaw the sample after it has been frozen for the polarization step, a solution exploited in previous DNP experiments [53].

7. External magnetic field

In principle, the class of protocols considered here, such as NOVEL or PulsePol, can operate at low magnetic field ($B_0 \lesssim 0.1$ T) as well as higher magnetic field (e.g., $B_0 \sim 5$ T), although the high field regime is substantially more technically demanding, requiring a high-power, high-frequency microwave source; similar to most conventional DNP methods.

The ability to operate at low fields therefore makes NV hyperpolarization potentially simpler and more cost effective than DNP. However, the subsequent measurement of the hyperpolarized sample in a high-field NMR spectrometer comes with its own challenges, and care must be taken to minimize polarization losses [69].

One requirement specific to the NV system is the need for the magnetic field to be aligned with the symmetry axis of the NV centers (within a few degrees), to ensure effective spin polarization by optical pumping [70]. The diamond hyperpolarizer must therefore be designed to facilitate this alignment, for instance (111)-oriented diamond surfaces [i.e., $\theta_{\mathrm{NV}} = 0$ in Fig. 2(b)] may prove easier to accommodate. Conveniently, $\theta_{\mathrm{NV}} = 0$ is the angle that gives the largest cooling rate [Fig. 4(b)].

IV. NV-BASED HYPERPOLARIZATION FOR NV-DETECTED NMR

We now turn our attention to the situation where the NMR signal is detected using a local magnetometer such as an NV center in the same diamond as that used for hyperpolarization, rather than with a remote inductive detector as in a conventional NMR spectrometer. The motivation is that the local polarization may be significantly larger than the average polarization, which suggests that the NMR signal detected by the NVs could be enhanced compared to the signal obtained in the absence of hyperpolarization.

Two scenarios are analyzed. In the first one, a layer of near-surface NV centers is used to generate the hyperpolarization but the NMR signal is detected by NV centers located deeper

in the diamond, typically several μm from the surface. This scenario, referred to as micro-NMR, could enable liquid-state NMR spectroscopy with a sensitivity and spectral resolution approaching that of conventional NMR, but with a greatly simplified apparatus. In the second scenario, referred to as nano-NMR, the same near-surface NV centers are used both for the hyperpolarization and for the NMR detection, which could find applications in NMR studies of nanoscale objects or NMR imaging with a sub-μm spatial resolution.

A. Micro-NMR

1. Background

In NV-based micro-NMR, as first demonstrated in Ref. [26], the NMR signal is read out by NV centers located several μm away from the sample (d_{RO}). The probe distance d_{RO} is chosen large enough so that diffusion of the nuclear spins in and out of the sensing volume (of size roughly given by d_{RO}) does not limit the NMR spectral resolution. For a liquid sample with diffusion coefficient D_n, the interaction correlation time due to translational diffusion is $\tau_c \approx \frac{2d_{\mathrm{RO}}^2}{D_n}$, which must be larger than the dephasing time of the nuclear spins $T_{2,n}^*$, in order to avoid spectral broadening [71]. For typical aqueous solutions, this implies $d_{\mathrm{RO}} \gtrsim 10$ μm [26,27].

NV-based NMR is generally conducted in a low magnetic field for experimental convenience. Since the NMR signal is proportional to the thermal polarization in this case, there is ample room for boosting the signal and hence the sensitivity by applying hyperpolarization techniques. For instance, the polarization was only $P_{\mathrm{th}} \approx 3 \times 10^{-7}$ in the original demonstration [26] ($B_0 = 88$ mT), which was later increased by more than two orders of magnitude by *in situ* liquid-state DNP based on the Overhauser effect [72]. Here we analyze the possibility of using NV centers to hyperpolarize the sample *in situ*, which would have the advantage of not having to introduce free radicals to the analyte.

A major drawback, however, is that NV hyperpolarization is not applicable to liquid samples, as we discussed in Sec. III C 3. One could envision increasing the viscosity of the solution, but $T_{2,n}^*$ would then decrease due to dipolar broadening, deteriorating the NMR linewidth. Moreover, in this case the distance d_{RO} could be reduced without compromising the spectral resolution, down to a few nanometers for $D_n \lesssim 10^{-14}$ m^2 s^{-1}. This corresponds to the nano-NMR regime analyzed in Sec. IV B. Thus, in order to combine NV hyperpolarization to liquid-state micro-NMR, it is necessary to freeze the solution for the polarization step (in principle, at any temperature below the freezing point) and then thaw it before the NMR measurement, as in dissolution DNP [52–54].

2. Model

Let us consider the configuration of Fig. 8(a). An array of near-surface NV centers (referred to as the HP-NVs), with a depth $d_{\mathrm{NV}} \sim 5$ nm and surface density σ_{HP}, is used to polarize the frozen-solution sample by applying the protocol described in Sec. II. Once the polarization has reached saturation, i.e., after a time $\sim T_{1,n}$, the sample is rapidly thawed and the NMR measurement can proceed using an array of readout NV centers (referred to as the RO-NVs) at a depth d_{RO}. We assume

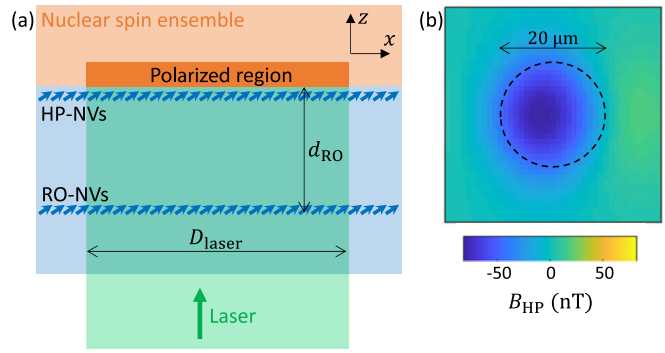

FIG. 8. (a) Proposed setup to combine liquid-state micro-NMR (using a layer of deep readout NVs, or RO-NVs) with *in situ* NV hyperpolarization (shallow NVs, or HP-NVs). (b) Calculated magnetic field amplitude B_{HP} produced by the polarized region in the plane of the RO-NVs for $d_{\mathrm{RO}} = 10$ μm. The dashed circle represents the laser beam of diameter $D_{\mathrm{laser}} = 20$ μm. The magnetization $\tilde{\mathbf{M}}_{\mathrm{HP}}$ was calculated from Eq. (21) assuming a density of HP-NVs $\sigma_{\mathrm{HP}} = 10^{16}$ m^{-2} and a number of polarized spins per HP-NV of $N_{\mathrm{s}} \approx 37\,000$ corresponding to the steady state polarization obtained from Sec. II with the following parameters: $\rho_n = 66$ nm^{-3}, $d_{\mathrm{NV}} = 5$ nm, $\theta_{\mathrm{NV}} = 54.7^\circ$, $T_{1,n} = 1$ s.

that the two NV arrays are excited by the same laser beam of diameter D_{laser}, with a typical value $D_{\mathrm{laser}} \approx 20$ μm [26].

The polarization step generates a disklike region of polarized sample of diameter $\approx D_{\mathrm{laser}}$. Because the probe distance d_{RO} is much larger than the extent of the polarization region from a single HP-NV ($\sim d_{\mathrm{NV}}$) and than the lateral separation between HP-NVs ($\sim \sigma_{\mathrm{HP}}^{-1/2}$), the stray field seen by the RO-NVs can be calculated by approximating the total polarized region as a thin disk of uniform magnetization. That is, we average out the spatial variations of the polarization over length scales much smaller than d_{RO}. The areal magnetization of this disk is then simply

$$\tilde{\mathbf{M}}_{\mathrm{HP}} = \sigma_{\mathrm{HP}} N_{\mathrm{s}} \mathbf{m}_n, \tag{21}$$

where N_{s} is the effective number of polarized spins due to a single HP-NV (as calculated in Sec. II C) and $\mathbf{m}_n$ is the magnetic moment of a single nuclear spin. The tilde in $\tilde{\mathbf{M}}_{\mathrm{HP}}$ denotes the fact that this is an areal magnetization (in units of A) rather than a volume magnetization (in A/m).

Upon thawing, the polarization will diffuse both laterally and vertically (away from the diamond surface). However, the spatial extent of this diffusion should be confined to a volume of the order of d_{RO} by the time the NMR measurement is completed, since this was the selection criterion for d_{RO}. One could also imagine to use the laser beam to induce the thawing process, in which case it might even be possible to keep a frozen containment structure surrounding the liquid core. In any case, we will assume for simplicity that the shape of the polarized region is approximately preserved upon thawing and throughout the NMR measurement.

Following an RF $\pi/2$ pulse, the magnetization precesses about the NV axis (unit vector $\mathbf{u}_{\mathrm{NV}}$), generating an AC magnetic field of amplitude B_{HP} at the position of a given RO-NV. B_{HP} is the projection of the field along the quantization axis of the RO-NV, i.e., $\mathbf{u}_{\mathrm{NV}}$. To calculate B_{HP}, we

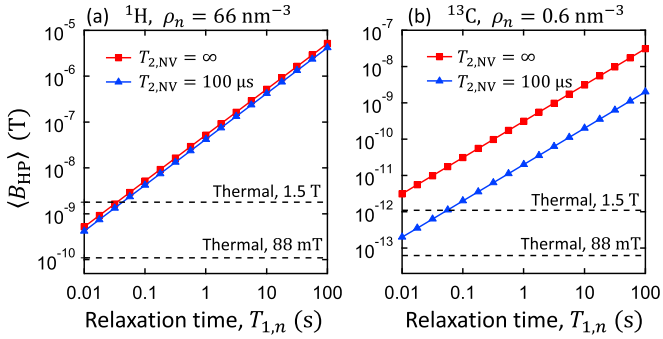

FIG. 9. (a) and (b) Average magnetic field seen by the RO-NVs as a result of hyperpolarization by the HP-NVs, $\langle B_{\rm HP}\rangle$, plotted as a function of the $T_{1,n}$ time of the target spins in the frozen phase. The sample is $\rho_n = 66$ nm^{-3} of ^{1}H spins in (a) and 1 M (or 0.6 nm^{-3}) of ^{13}C spins in (b). The magnetization $\tilde{\mathbf{M}}_{\rm HP}$ is calculated assuming $\sigma_{\rm HP} = 10^{16}$ m^{-2}, $d_{\rm NV} = 5$ nm, $\theta_{\rm NV} = 54.7^\circ$, and $T_{2,\rm NV} = \infty$ (red data) or $T_{2,\rm NV} = 100$ μs (blue). The stray field $\langle B_{\rm HP}\rangle$ is calculated assuming $d_{\rm RO} = 10$ μm and $D_{\rm laser} = 20$ μm. The dashed lines indicate the field amplitude seen by the RO-NVs due to thermal polarization only, at a field $B_0 = 1.5$ T or $B_0 = 88$ mT.

compute the stray field generated by a magnetic disk of magnetization $\tilde{\mathbf{M}}_{\rm HP}$ given by Eq. (21), where we choose the direction of $\mathbf{m}_n$ that maximizes the field seen by the RO-NVs. For instance, if $\mathbf{u}_{\rm NV}$ lies in the xz plane, i.e., $\mathbf{u}_{\rm NV} = (\sin\theta_{\rm NV}, 0, \cos\theta_{\rm NV})$ in Cartesian coordinates, we take $\mathbf{m}_n = \frac{\hbar\gamma_n}{2}\mathbf{u}_y \times \mathbf{u}_{\rm NV} = \frac{\hbar\gamma_n}{2}(\cos\theta_{\rm NV}, 0, -\sin\theta_{\rm NV})$.

3. Results

As an example, Fig. 8(b) shows the calculated $B_{\rm HP}$ amplitude in the plane of the RO-NVs at $d_{\rm RO} = 10$ μm, from a polarized region of diameter $D_{\rm laser} = 20$ μm, with an NV angle $\theta_{\rm NV} = 54.7^\circ$. In these simulations the HP-NV layer is characterized by $d_{\rm NV} = 5$ nm and $\sigma_{\rm HP} = 10^{16}$ m^{-2}, and the sample mimics frozen water (^{1}H spins with $\rho_n = 66$ nm^{-3} and $T_{1,n} = 1$ s). Averaging $B_{\rm HP}$ over the readout disk [dashed circle in Fig. 8(b)], we obtain $\langle B_{\rm HP}\rangle \approx 42$ nT in this case.

The average field $\langle B_{\rm HP}\rangle$ is proportional to the amplitude of $\tilde{\mathbf{M}}_{\rm HP}$ hence scales as $\langle B_{\rm HP}\rangle \propto \sigma_{\rm HP}\gamma_n\rho_n^{1/2}d_{\rm NV}^{-3/2}T_{1,n}$, where $T_{1,n}$ is the longitudinal spin relaxation time in the frozen phase. To illustrate the range of fields one could obtain, Fig. 9 plots $\langle B_{\rm HP}\rangle$ as a function of $T_{1,n}$ for a solution with a high density of ^{1}H spins [Fig. 9(a)] and for 1 M of ^{13}C spins [Fig. 9(b)]. The hyperpolarization step assumes $\sigma_{\rm HP} = 10^{16}$ m^{-2}, $d_{\rm NV} = 5$ nm, and $T_{2,\rm NV} = \infty$ (red data) or $T_{2,\rm NV} = 100$ μs (blue).

The values obtained can be compared to the field amplitude $B_{\rm th}$ that would be obtained from thermal polarization only. The volume magnetization is

$$\mathbf{M}_{\rm th} = \rho_n P_{\rm th}\mathbf{m}_n, \tag{22}$$

where $P_{\rm th}$ is given by Eq. (17). In general, the stray field $B_{\rm th}$ depends on the portion of sample contributing to the magnetization $\mathbf{M}_{\rm th}$, which depends on technical details such as the homogeneity of the RF driving field. Nevertheless, if the corresponding volume has a size much larger than $d_{\rm RO}$ and $D_{\rm laser}$, as is typically the case, then $B_{\rm th}$ is uniform in the RO-NV plane and depends little on the exact volume and shape of the active part of the sample [27]. For simplicity we will therefore consider a sample of cubic shape, for which the stray field can be calculated analytically. The resulting field is indicated by dashed lines in Figs. 9(a) and 9(b), where we show the cases $B_0 = 88$ mT (similar to Ref. [26]) and $B_0 = 1.5$ T (similar to the prepolarization stage in Ref. [27]).

For the high density ^{1}H solution [Fig. 9(a)], we see that with a modest value of $T_{1,n} = 1$ s, $\langle B_{\rm HP}\rangle$ exceeds $B_{\rm th}$ by a factor $\approx$400 at 88 mT, and by a factor $\approx$20 at 1.5 T, with a negligible reduction caused by a finite $T_{2,\rm NV}$. Assuming the freeze-thaw process can be repeated many times, with a hyperpolarization time ($\sim T_{1,n}$) of the same order as the measurement time (assuming $T_{2,n}^* \sim T_{1,n}$ which is plausible for a liquid), the temporal overhead could be just a few seconds (including freezing and thawing times) for $\sim$1 s of measurement. In this case, the signal enhancement $\langle B_{\rm HP}\rangle/B_{\rm th}$ would translate into a comparable level of SNR enhancement, suggesting that NV hyperpolarization could be viable in this scenario.

A relatively straightforward improvement could come from structuring the diamond surface to form a nanograting, as demonstrated in Ref. [73]. This would effectively increase the NV surface density $\sigma_{\rm HP}$, translating into an increase in $\langle B_{\rm HP}\rangle$ by the same amount. A 15-fold increase in $\sigma_{\rm HP}$ was demonstrated in Ref. [73], and even larger enhancements can be anticipated with higher aspect ratios [36–40].

For a solution containing 1 M of ^{13}C spins [Fig. 9(b)], the enhancement $\langle B_{\rm HP}\rangle/B_{\rm th}$ is larger in the ideal case, but is reduced by an order of magnitude when taking into account $T_{2,\rm NV} = 100$ μs, which is due to the fact that the flip-flop time is now longer ($\tau_0 \approx 1.2$ ms). Nevertheless, with this finite $T_{2,\rm NV} = 100$ μs we still predict a 300-fold enhancement over $B_{\rm th}$ at 88 mT with $T_{1,n} = 1$ s.

B. Nano-NMR

1. Background

We now consider the possibility of using NV hyperpolarization to benefit nano-NMR or nano-MRI experiments. Here we refer to the use of a single near-surface NV center (typically, $d_{\rm NV} \lesssim 10$ nm) to perform NMR spectroscopy on a nanoscale volume of order $d_{\rm NV}^3$ [28,29,74,75] ("nano-NMR"), or the use of a dense two-dimensional layer of near-surface NV centers to image the nano-NMR signal on a camera [66,76] ("nano-MRI"). Nano-NMR may be useful to study surface interactions and the dynamics of molecules at the nanoscale through the analysis of correlations in the NMR signal [67] or to characterize interactions in nanoscale materials [77], whereas nano-MRI allows characterization of samples over larger scales, with a submicrometer lateral spatial resolution (limited by optical diffraction).

Previous demonstrations of nano-NMR/MRI have used the NVs to detect the statistical polarization of the nuclear spins [28,29,74,75], as it is much larger than the thermal (Boltzmann) polarization for nanoscale volumes. Statistical polarization spontaneously generates a magnetic field oscillating at the Larmor frequency of the nuclear spins. Because the phase of this oscillating field is random, time-averaged NV measurements are sensitive to the variance of this field $B_{\rm rms}^2$

which is given by [71]

$$B_{\rm rms}^2 = \rho_n \left(\frac{\mu_0 \hbar \gamma_n}{4\pi}\right)^2 \frac{\pi[8 - 3\sin^4(\theta_{\rm NV})]}{128 d_{\rm NV}^3} \tag{23}$$

in the geometry of Fig. 2(b).

While there are several ways to generate an NMR spectrum [28,29,78], they all produce a measurable "signal" (namely, a change in NV spin population) of the order of $\Delta p_{\rm NV}^{\rm rms} \sim (\gamma_e B_{\rm rms} \tau_{\rm sens})^2$ in the small signal limit, where $\tau_{\rm sens}$ is the interrogation (sensing) time, which is limited by the NV coherence time $T_{2,\rm NV}$. For a dense ensemble of ^{1}H spins ($\rho_n = 66$ nm^{-3}), with an NV at $d_{\rm NV} = 5$ nm and $\theta_{\rm NV} = 54.7°$, we obtain $B_{\rm rms} \approx 830$ nT, giving a nearly full contrast ($\Delta p_{\rm NV}^{\rm rms} \sim 1$) in only $\tau_{\rm sens} \sim 10$ μs, which is typically well within $T_{2,\rm NV}$. For a more dilute sample ($\rho_n = 0.6$ nm^{-3}), however, $B_{\rm rms} \approx 80$ nT which gives only $\Delta p_{\rm NV}^{\rm rms} \sim 10^{-2}$ with $\tau_{\rm sens} \sim 10$ μs.

On the other hand, NV hyperpolarization followed by a $\pi/2$ RF pulse on the nuclear spins would generate a signal of the form $\Delta p_{\rm NV}^{\rm HP} \sim \gamma_e B_{\rm HP} \tau_{\rm sens}$, where $B_{\rm HP}$ is the amplitude of the AC magnetic field from the polarized spins, evaluated at the NV location [79]. This amplitude can be computed as the sum of the dipolar field from each nuclear spin, projected along the NV axis,

$$B_{\rm HP} = \rho_n \int P(\mathbf{R}, \infty) \mathbf{b}_{\rm AC}(\mathbf{R}) \cdot \mathbf{u}_{\rm NV} \, d^3\mathbf{R}, \tag{24}$$

with

$$\mathbf{b}_{\rm AC}(\mathbf{R}) = \frac{\mu_0}{4\pi}\left(\frac{3(\mathbf{m}_n \cdot \mathbf{R})\mathbf{R}}{R^5} - \frac{\mathbf{m}_n}{R^3}\right), \tag{25}$$

where $\mathbf{u}_{\rm NV}$ is the NV axis unit vector, $\mathbf{m}_n$ is the magnetic moment of the nuclear spins in the transverse position that maximizes $B_{\rm HP}$, and $P(\mathbf{R}, \infty)$ is the steady-state polarization distribution, solution of Eq. (8).

In nano-MRI applications where a dense layer of NV centers is addressed at once, the polarization distribution should include the effect of all the NVs in the array. However, we found that the dominant contribution to $B_{\rm HP}$ at a given NV site comes from the polarization imparted by this same NV, with a negligible contribution from the neighboring NVs even at NV densities as large as $\sigma_{\rm HP} = 10^{16}$ m^{-2}. Therefore, for generality the results below present the single NV limit.

2. Results

To compare the amplitude $B_{\rm HP}$ obtained from NV hyperpolarization with $B_{\rm rms}$, we plot the ratio $B_{\rm HP}/B_{\rm rms}$ as a function of $T_{1,n}$ for a semi-infinite ensemble of ^{1}H spins [Fig. 10(a)]. Two densities are compared, $\rho_n = 66$ nm^{-3} (red data) and $\rho_n = 0.6$ nm^{-3} (blue), and a diffusion coefficient corresponding to the solid-state case, $D_n \approx 0.22 \frac{\mu_0}{4\pi} \hbar \gamma_n^2 \rho_n^{1/3}$ [35], is included. The other parameters are taken as $d_{\rm NV} = 5$ nm, $\theta_{\rm NV} = 54.7°$, and $T_{2,\rm NV} = 1$ ms. The ratio $B_{\rm HP}/B_{\rm rms}$ is found to vary relatively weakly with $T_{1,n}$, in a roughly logarithmic manner. We have $B_{\rm HP}/B_{\rm rms} \sim 1$ for $T_{1,n} = 10$ ms, increasing to $B_{\rm HP}/B_{\rm rms} \approx 8$ for the dilute sample when $T_{1,n} = 10$ s and only $B_{\rm HP}/B_{\rm rms} \approx 4$ for the dense sample. This weak dependence can be understood by considering the role of diffusion: even though the total number of polarized spins $N_{\rm s}$ increases linearly with $T_{1,n}$ [Eq. (13)], this polarization extends further away from the NV spin on average thus causing a comparatively small increase in the local magnetic field seen by the NV; this effect is more marked in the dense sample when diffusion is faster.

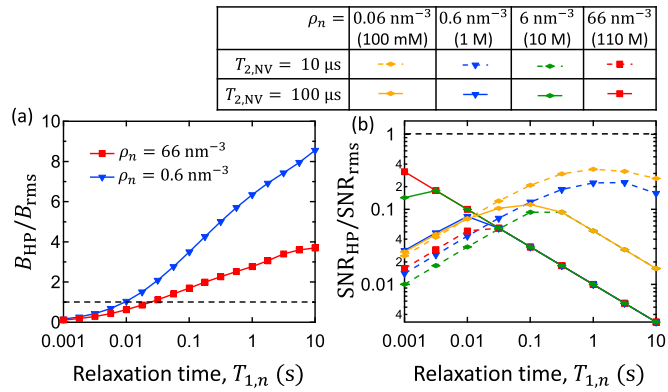

FIG. 10. (a) Calculated ratio $B_{\rm HP}/B_{\rm rms}$ as a function of $T_{1,n}$ for ^{1}H spins with $\rho_n = 66$ nm^{-3} (red data, $B_{\rm rms} \approx 830$ nT) and $\rho_n = 0.6$ nm^{-3} (blue, $B_{\rm rms} \approx 80$ nT). Diffusion is included with a coefficient $D_n = 0.22 \frac{\mu_0}{4\pi} \hbar \gamma_n^2 \rho_n^{1/3}$. Other parameters are: $d_{\rm NV} = 5$ nm, $\theta_{\rm NV} = 54.7°$, $T_{2,\rm NV} = 1$ ms. (b) Calculated ratio $\rm SNR_{HP}/SNR_{rms}$ [from Eq. (27)] as a function of $T_{1,n}$ for ^{1}H spins with $\rho_n = 66$ nm^{-3} (red data), $\rho_n = 6$ nm^{-3} (green), $\rho_n = 0.6$ nm^{-3} (blue), and $\rho_n = 0.06$ nm^{-3} (orange). The NV coherence time is $T_{2,\rm NV} = 10$ μs (dashed lines) or 100 μs (solid lines). The correlation time of the AC field is taken to be $\tau_c = 100$ μs. Other parameters are as in (a).

We now examine how the SNR would change in an experiment detecting $B_{\rm HP}$ following NV hyperpolarization, compared to simply detecting $B_{\rm rms}$. In most NV experiments, the noise scales as $T_{\rm meas}^{-1/2}$ where $T_{\rm meas}$ is the time dedicated to the NV measurement which can be written as $T_{\rm meas} = \beta T$ where T is the total experimental time and β is the duty cycle of the measurement, which depends on the details of the experiment including readout time, dead times, etc [80]. For the same total time T, the SNR ratio is then

$$\frac{\rm SNR_{HP}}{\rm SNR_{rms}} = \frac{\Delta p_{\rm NV}^{\rm HP}}{\Delta p_{\rm NV}^{\rm rms}} \sqrt{\frac{\beta_{\rm HP}}{\beta_{\rm rms}}} \sim \frac{\gamma_e B_{\rm HP} \tau_{\rm sens}^{\rm HP}}{\left(\gamma_e B_{\rm rms} \tau_{\rm sens}^{\rm rms}\right)^2} \sqrt{\frac{\beta_{\rm HP}}{\beta_{\rm rms}}}, \tag{26}$$

which captures the ratio of the signal and the ratio of the noise based on the above discussion, with $\beta_{\rm HP}$ ($\beta_{\rm rms}$) the duty cycle for the hyperpolarized (statistically polarized) case. In Eq. (26) $\tau_{\rm sens}^{\rm HP,rms}$ is the optimum sensing time for each case, which we take to be $\tau_{\rm sens} = T_{2,\rm NV}$ or the $\tau_{\rm sens}$ giving $\Delta p_{\rm NV} = 1$, whichever is shortest. This ensures that the signal is not greater than it can be in reality.

Because of the different exponents, the ratio of signals $\frac{\Delta p_{\rm NV}^{\rm HP}}{\Delta p_{\rm NV}^{\rm rms}}$ can easily exceed unity even when $B_{\rm HP}$ is comparable to or smaller than $B_{\rm rms}$. However, the ratio of the duty cycles is generally very unfavorable to the hyperpolarization pathway. Indeed, in this case the experimental sequence adds a polarization step (which takes $\sim T_{1,n}$) and a $\pi/2$ RF pulse (10's of μs, neglected in what follows) before each NV measurement. The duration of a single measurement is limited by the correlation time of the AC magnetic field, which is typically in the

range $\tau_c \sim 10$–$100\ \mu$s for shallow NV centers ($d_{\mathrm{NV}} \sim 5$ nm) both for solid and liquid samples [67]. This means that the measurement would take up only a fraction $\beta_{\mathrm{HP}} \sim \frac{\tau_c}{T_{1,n}}$ of the total time. Assuming β_{rms} is close to unity, we obtain

$$\frac{\mathrm{SNR}_{\mathrm{HP}}}{\mathrm{SNR}_{\mathrm{rms}}} \sim \frac{\gamma_e B_{\mathrm{HP}} \tau_{\mathrm{sens}}^{\mathrm{HP}}}{\left(\gamma_e B_{\mathrm{rms}} \tau_{\mathrm{sens}}^{\mathrm{rms}}\right)^2} \sqrt{\frac{\tau_c}{T_{1,n}}}. \tag{27}$$

Given that B_{HP} increases with increasing $T_{2,\mathrm{NV}}$ and $T_{1,n}$, one can expect a maximum for $\frac{\mathrm{SNR}_{\mathrm{HP}}}{\mathrm{SNR}_{\mathrm{rms}}}$ as a function of these parameters. This is explored in Fig. 10(b), which plots the SNR ratio as a function of $T_{1,n}$ for different densities ρ_n and different NV coherence times $T_{2,\mathrm{NV}}$, assuming a correlation time $\tau_c = 100\ \mu$s. The SNR ratio is always below 1, showing that the increased signal is not sufficient to overcome the increased noise. The most promising regime is that of small densities, e.g., $\rho_n = 0.06\ \mathrm{nm}^{-3}$, i.e., 100 mM, and short coherence times, e.g., $T_{2,\mathrm{NV}} = 10\ \mu$s, for which the magnetic fields are small hence the ratio of signals can be quite large, in the range 10–100. On the other hand, large densities and long $T_{2,\mathrm{NV}}$ means that the signals are often saturated, $\Delta p_{\mathrm{NV}}^{\mathrm{AC}} \sim \Delta p_{\mathrm{NV}}^{\mathrm{rms}} \sim 1$, which leads to an SNR ratio $\ll 1$.

We also examined the case of a sample confined in the vertical direction, instead of semi-infinite sample as assumed before. This could apply, for instance, to a lipid bilayer (a few nanometers thick) [81] or an atomically thin van der Waals material [77]. In this case, the polarization extends further in the lateral directions (parallel to the diamond surface), however, we found that the magnetic field B_{HP} seen by the NV remains relatively unchanged. On the other hand, confinement in three dimensions can have a measurable effect. For example, a $10 \times 10 \times 5\ \mathrm{nm}^3$ sample positioned above the NV would generate a field B_{HP} larger by a factor ≈ 10 compared to a semi-infinite sample, assuming ^{1}H spins with $\rho_n = 66\ \mathrm{nm}^{-3}$, $d_{\mathrm{NV}} = 5$ nm, and $\theta_{\mathrm{NV}} = 54.7^\circ$. Nevertheless, the SNR ratio $\frac{\mathrm{SNR}_{\mathrm{HP}}}{\mathrm{SNR}_{\mathrm{rms}}}$ remains below unity in all cases.

We note that the spectral resolution in nano-NMR experiments is also unlikely to be improved by NV hyperpolarization. Indeed, the spectral resolution is limited by the correlation time τ_c of the oscillating/fluctuating magnetic field detected by the NV, which is expected to be similar whether it is the fluctuating field from statistical polarization or the AC field from net polarization. This resolution limit can be readily reached through correlation spectroscopy for statistical polarization [67,75,78], and through FID-like measurements for net polarization [26]. For solid samples, τ_c is given by the dephasing time of the nuclear spins ($T_{2,n}^*$), which is governed by dipolar interactions. In conventional solid-state NMR, this dipolar broadening is often efficiently removed by magic-angle spinning and homo- or heteronuclear decoupling sequences, but in principle these methods can be applied to statistical polarization as well [75].

V. CONCLUSION

In this work we theoretically investigated several potential applications of nuclear spin hyperpolarization based on optically pumped NV centers in diamond. We first analyzed the possibility of using NV hyperpolarization to polarize a macroscopic sample that would then be measured in a conventional NMR spectrometer. We found that, for NV hyperpolarization to be competitive with existing hyperpolarization techniques, a key condition is to specially engineer the diamond structure to maximize the contact area between NVs and sample. We predicted, assuming optimally efficient polarization transfer, that enhancements over thermal polarization by up to two orders of magnitude can be obtained with existing technology. Larger enhancements, equivalent to polarizations exceeding 10%, can in principle be obtained but this requires structuring the diamond with aspect ratios of over a hundred, which is an outstanding challenge. We discussed factors reducing the polarization transfer efficiency, especially the finite NV spin coherence time, which motivates further work in the optimization of diamond materials. In particular, doping engineering [56–58] and optimized annealing [59] are promising strategies to jointly improve the NV yield and minimize parasitic noise, which could lead to significant performance improvements. We also outlined some of the practical challenges of NV hyperpolarization, such as the need for high power laser illumination, and the requirement that the sample be in a solid form for the hyperpolarization step. Overall, this application emerges as challenging, but the prospect of realizing a versatile, noninvasive hyperpolarization platform at a fraction of the cost of existing techniques warrants further work. In this context, searching for new solid-state spin systems is a particularly relevant research direction, as it might lead to a system with more favorable attributes than the NV for this application, e.g., by allowing higher areal spin densities, closer to the surface, or requiring less laser intensity.

Next, we examined the possibility of integrating NV hyperpolarization into NV-based liquid-state micro-NMR. NV-based micro-NMR is a recently developed technique [26] that could lead to the realization of portable NMR spectrometers. The technique relies on NV centers located several μm away from the diamond surface, which limits the NMR sensitivity. We found that, by adding a layer of near-surface NV centers to hyperpolarize the sample, a signal boost of about 1–2 orders of magnitude over thermal polarization can be obtained in principle, with further enhancements expected with microstructuring of the diamond surface. Thus, built-in NV hyperpolarization could prove a convenient way to boost the sensitivity of NV micro-NMR, without the inconvenience of conventional DNP which requires adding free radicals to the solution [72]. One drawback of NV hyperpolarization, however, is the need to freeze the sample for the hyperpolarization step, which adds a technical complication and may not be desirable/possible for some samples. It should also be noted that our predictions are based on a simplistic model where the polarization distribution is assumed to be unchanged upon thawing of the sample. Further work will be required to test more sophisticated models taking into account polarization diffusion during the NMR measurement in the liquid state.

Finally, we analyzed the case of nano-NMR, where near-surface NV centers are normally employed to detect the randomly fluctuating magnetic field induced by statistical polarization. We found that using the same NV to hyperpolarize the sample and measure the net polarization instead can lead to an increase in the measurable signal. However, this generally does not translate into a net improvement in

the signal-to-noise ratio of the measurement because of the significant temporal overhead of the hyperpolarization step, which dominates the comparatively short measurement time typically involved in nano-NMR experiments. Thus, NV hyperpolarization for nano-NMR seems to be the least promising application, although future work could look at techniques that may mitigate the impact of the temporal overhead, such as quantum-memory-assisted repetitive readout schemes [74,82].

Another area of interest for future work is the possibility to make the polarization transfer more efficient by exploiting a different pathway to the direct NV-sample coupling studied here. For instance, Ref. [83] theoretically investigated the possibility of exploiting ancillary electron spins to enhance the coupling, which in effect amounts to reducing the NV-target distance. Another intriguing idea is to use the natural bath of ^{13}C spins present inside the diamond as a polarization buffer [20]. In this scheme, a single NV spin would polarize a large number of those internal ^{13}C spins over the course of minutes to hours (limited by the longitudinal relaxation time of ^{13}C in diamond), and this internal ^{13}C polarization would then be transferred to (or spontaneously diffuse towards) the target nuclear spins located outside the diamond. Assuming the target spins have a much shorter $T_{1,n}$ time than the internal ^{13}C, this amounts to increasing the density of polarizing agents in the diamond from the NV density ($\sim$10 ppm) to the internal ^{13}C density (1.1% for natural isotopic concentration), i.e., a 100-fold increase. However, further work is required to quantify the potential of this approach in realistic conditions.

ACKNOWLEDGMENTS

We acknowledge support from the Australian Research Council (ARC) through Grants DE170100129, CE170100012, and DP190101506. A.J.H. is supported by an Australian Government Research Training Program Scholarship.

[1] J. H. Lee, Y. Okuno, and S. Cavagnero, Sensitivity enhancement in solution NMR: Emerging ideas and new frontiers, J. Magn. Reson. **241**, 18 (2014), a special "JMR Perspectives" issue: Foresights in Biomolecular Solution-State NMR Spectroscopy - From Spin Gymnastics to Structure and Dynamics.

[2] T. G. Walker and W. Happer, Spin-exchange optical pumping of noble-gas nuclei, Rev. Mod. Phys. **69**, 629 (1997).

[3] G. Navon, Y.-Q. Song, T. Rõõm, S. Appelt, R. E. Taylor, and A. Pines, Enhancement of solution NMR and MRI with laser-polarized xenon, Science **271**, 1848 (1996).

[4] J. Natterer and J. Bargon, Parahydrogen induced polarization, Prog. Nucl. Magn. Reson. Spectrosc. **31**, 293 (1997).

[5] J.-B. Hövener, A. N. Pravdivtsev, B. Kidd, C. R. Bowers, S. Glöggler, K. V. Kovtunov, M. Plaumann, R. Katz-Brull, K. Buckenmaier, A. Jerschow, F. Reineri, T. Theis, R. V. Shchepin, S. Wagner, P. Bhattacharya, N. M. Zacharias, and E. Y. Chekmenev, Parahydrogen-based hyperpolarization for biomedicine, Angew. Chem., Int. Ed. **57**, 11140 (2018).

[6] A. Abragam and M. Goldman, Principles of dynamic nuclear polarisation, Rep. Prog. Phys. **41**, 395 (1978).

[7] R. Wind, M. Duijvestijn, C. van der Lugt, A. Manenschijn, and J. Vriend, Applications of dynamic nuclear polarization in 13C NMR in solids, Prog. Nucl. Magn. Reson. Spectrosc. **17**, 33 (1985).

[8] D. A. Hall, D. C. Maus, G. J. Gerfen, S. J. Inati, L. R. Becerra, F. W. Dahlquist, and R. G. Griffin, Polarization-enhanced NMR spectroscopy of biomolecules in frozen solution, Science **276**, 930 (1997).

[9] K. Tateishi, M. Negoro, S. Nishida, A. Kagawa, Y. Morita, and M. Kitagawa, Room temperature hyperpolarization of nuclear spins in bulk, Proc. Natl. Acad. Sci. **111**, 7527 (2014).

[10] M.-A. Sani, S. Zhu, V. Hofferek, and F. Separovic, Nitroxide spin-labeled peptides for DNP-NMR in-cell studies, FASEB J. **33**, 11021 (2019).

[11] D. A. Broadway, J.-P. Tetienne, A. Stacey, J. D. A. Wood, D. A. Simpson, L. T. Hall, and L. C. L. Hollenberg, Quantum probe hyperpolarisation of molecular nuclear spins, Nat. Commun. **9**, 1246 (2018).

[12] P. Fernández-Acebal, O. Rosolio, J. Scheuer, C. Müller, S. Müller, S. Schmitt, L. McGuinness, I. Schwarz, Q. Chen, A. Retzker, B. Naydenov, F. Jelezko, and M. Plenio, Toward hyperpolarization of oil molecules via single nitrogen vacancy centers in diamond, Nano Lett. **18**, 1882 (2018).

[13] F. Shagieva, S. Zaiser, P. Neumann, D. B. R. Dasari, R. Stöhr, A. Denisenko, R. Reuter, C. A. Meriles, and J. Wrachtrup, Microwave-assisted cross-polarization of nuclear spin ensembles from optically pumped nitrogen-vacancy centers in diamond, Nano Lett. **18**, 3731 (2018).

[14] A. Henstra and W. Wenckebach, The theory of nuclear orientation via electron spin locking (novel), Mol. Phys. **106**, 859 (2008).

[15] P. London, J. Scheuer, J.-M. Cai, I. Schwarz, A. Retzker, M. B. Plenio, M. Katagiri, T. Teraji, S. Koizumi, J. Isoya, R. Fischer, L. P. McGuinness, B. Naydenov, and F. Jelezko, Detecting and Polarizing Nuclear Spins with Double Resonance on a Single Electron Spin, Phys. Rev. Lett. **111**, 067601 (2013).

[16] J. P. King, P. J. Coles, and J. A. Reimer, Optical polarization of ^{13}C nuclei in diamond through nitrogen vacancy centers, Phys. Rev. B **81**, 073201 (2010).

[17] G. A. Álvarez, C. O. Bretschneider, R. Fischer, P. London, H. Kanda, S. Onoda, J. Isoya, D. Gershoni, and L. Frydman, Local and bulk 13C hyperpolarization in nitrogen-vacancy-centered diamonds at variable fields and orientations, Nat. Commun. **6**, 8456 (2015).

[18] J. P. King, K. Jeong, C. C. Vassiliou, C. S. Shin, R. H. Page, C. E. Avalos, H.-J. Wang, and A. Pines, Room-temperature in situ nuclear spin hyperpolarization from optically pumped nitrogen vacancy centers in diamond, Nat. Commun. **6**, 8965 (2015).

[19] D. Pagliero, K. R. K. Rao, P. R. Zangara, S. Dhomkar, H. H. Wong, A. Abril, N. Aslam, A. Parker, J. King, C. E. Avalos, A. Ajoy, J. Wrachtrup, A. Pines, and C. A. Meriles, Multispin-assisted optical pumping of bulk ^{13}C nuclear

spin polarization in diamond, Phys. Rev. B **97**, 024422 (2018).

[20] A. Ajoy, K. Liu, R. Nazaryan, X. Lv, P. R. Zangara, B. Safvati, G. Wang, D. Arnold, G. Li, A. Lin, P. Raghavan, E. Druga, S. Dhomkar, D. Pagliero, J. A. Reimer, D. Suter, C. A. Meriles, and A. Pines, Orientation-independent room temperature optical 13C hyperpolarization in powdered diamond, Sci. Adv. **4**, eaar5492 (2018).

[21] J. Henshaw, D. Pagliero, P. R. Zangara, M. B. Franzoni, A. Ajoy, R. H. Acosta, J. A. Reimer, A. Pines, and C. A. Meriles, Carbon-13 dynamic nuclear polarization in diamond via a microwave-free integrated cross effect, Proc. Natl. Acad. Sci. **116**, 18334 (2019).

[22] J. Scheuer, I. Schwartz, S. Müller, Q. Chen, I. Dhand, M. B. Plenio, B. Naydenov, and F. Jelezko, Robust techniques for polarization and detection of nuclear spin ensembles, Phys. Rev. B **96**, 174436 (2017).

[23] I. Schwartz, J. Scheuer, B. Tratzmiller, S. Müller, Q. Chen, I. Dhand, Z.-Y. Wang, C. Müller, B. Naydenov, F. Jelezko, and M. B. Plenio, Robust optical polarisation of nuclear spin baths using Hamiltonian engineering of NV centre quantum dynamics, Sci. Adv. **4**, eaat8978 (2018).

[24] Y. Hovav, B. Naydenov, F. Jelezko, and N. Bar-Gill, Low-Field Nuclear Polarization Using Nitrogen Vacancy Centers in Diamonds, Phys. Rev. Lett. **120**, 060405 (2018).

[25] J. E. Lang, D. A. Broadway, G. A. L. White, L. T. Hall, A. Stacey, L. C. L. Hollenberg, T. S. Monteiro, and J.-P. Tetienne, Quantum Bath Control with Nuclear Spin State Selectivity Via Pulse-Adjusted Dynamical Decoupling, Phys. Rev. Lett. **123**, 210401 (2019).

[26] D. R. Glenn, D. B. Bucher, J. Lee, M. D. Lukin, H. Park, and R. L. Walsworth, High-resolution magnetic resonance spectroscopy using a solid-state spin sensor, Nature (London) **555**, 351 (2018).

[27] J. Smits, J. T. Damron, P. Kehayias, A. F. McDowell, N. Mosavian, I. Fescenko, N. Ristoff, A. Laraoui, A. Jarmola, and V. M. Acosta, Two-dimensional nuclear magnetic resonance spectroscopy with a microfluidic diamond quantum sensor, Sci. Adv. **5**, eaaw7895 (2019).

[28] T. Staudacher, F. Shi, S. Pezzagna, J. Meijer, J. Du, C. a. Meriles, F. Reinhard, and J. Wrachtrup, Nuclear magnetic resonance spectroscopy on a (5-nanometer)^3 sample volume, Science **339**, 561 (2013).

[29] H. J. Mamin, M. Kim, M. H. Sherwood, C. T. Rettner, K. Ohno, D. D. Awschalom, and D. Rugar, Nanoscale nuclear magnetic resonance with a nitrogen-vacancy spin sensor, Science **339**, 557 (2013).

[30] A. Jarmola, V. M. Acosta, K. Jensen, S. Chemerisov, and D. Budker, Temperature- and Magnetic-Field-Dependent Longitudinal Spin Relaxation in Nitrogen-Vacancy Ensembles in Diamond, Phys. Rev. Lett. **108**, 197601 (2012).

[31] N. Bar-Gill, L. M. Pham, a. Jarmola, D. Budker, and R. L. Walsworth, Solid-state electronic spin coherence time approaching one second, Nat. Commun. **4**, 1743 (2013).

[32] L. T. Hall, D. A. Broadway, A. Stacey, D. A. Simpson, J.-P. Tetienne, and L. C. L. Hollenberg, Maximising dynamic nuclear polarisation via selective hyperfine tuning, arXiv:2012.12508.

[33] M. Kaviani, P. Deák, B. Aradi, T. Frauenheim, J.-P. Chou, and A. Gali, Proper surface termination for luminescent near-surface NV centers in diamond, Nano Lett. **14**, 4772 (2014).

[34] M. Loretz, S. Pezzagna, J. Meijer, and C. L. Degen, Nanoscale nuclear magnetic resonance with a 1.9-nm-deep nitrogen-vacancy sensor, Appl. Phys. Lett. **104**, 033102 (2014).

[35] T. T. P. Cheung, Spin diffusion in NMR in solids, Phys. Rev. B **23**, 1404 (1981).

[36] P. Forsberg and M. Karlsson, High aspect ratio optical gratings in diamond, Diam. Relat. Mater. **34**, 19 (2013).

[37] E. Vargas Catalan, P. Forsberg, O. Absil, and M. Karlsson, Controlling the profile of high aspect ratio gratings in diamond, Diam. Relat. Mater. **63**, 60 (2016).

[38] K. Li, Y. Liu, M. Seaberg, M. Chollet, T. M. Weiss, and A. Sakdinawat, Wavefront preserving and high efficiency diamond grating beam splitter for x-ray free electron laser, Opt. Express **28**, 10939 (2020).

[39] Y. Yang, M.-F. Yuen, X. Chen, S. Xu, Y. Tang, and W. Zhang, Fabrication of arrays of high-aspect-ratio diamond nanoneedles via maskless ECR-assisted microwave plasma etching, Cryst. Eng. Commun. **17**, 2791 (2015).

[40] K. Li, Fabrication of high aspect ratio silicon and diamond for x-ray optics (Conference Presentation), in *Nanoengineering: Fabrication, Properties, Optics, and Devices XV*, Vol. 10730, edited by B. Panchapakesan, A. E. Sakdinawat, A.-J. Attias, and E. A. Dobisz, International Society for Optics and Photonics (SPIE, Bellingham, WA, 2018).

[41] L. Rondin, G. Dantelle, a. Slablab, F. Grosshans, F. Treussart, P. Bergonzo, S. Perruchas, T. Gacoin, M. Chaigneau, H. C. Chang, V. Jacques, and J. F. Roch, Surface-induced charge state conversion of nitrogen-vacancy defects in nanodiamonds, Phys. Rev. B **82**, 115449 (2010).

[42] https://www.adamasnano.com/functionalized-fluorescent-bioprobes.

[43] J.-P. Tetienne, T. Hingant, L. Rondin, A. Cavaillès, L. Mayer, G. Dantelle, T. Gacoin, J. Wrachtrup, J.-F. Roch, and V. Jacques, Spin relaxometry of single nitrogen-vacancy defects in diamond nanocrystals for magnetic noise sensing, Phys. Rev. B **87**, 235436 (2013).

[44] L. Robledo, H. Bernien, T. V. D. Sar, and R. Hanson, Spin dynamics in the optical cycle of single nitrogen-vacancy centres in diamond, New J. Phys. **13**, 025013 (2011).

[45] D. Bluvstein, Z. Zhang, and A. C. B. Jayich, Identifying and Mitigating Charge Instabilities in Shallow Diamond Nitrogen-Vacancy Centers, Phys. Rev. Lett. **122**, 076101 (2019).

[46] S. Dhomkar, H. Jayakumar, P. R. Zangara, and C. A. Meriles, Charge dynamics in near-surface, variable-density ensembles of nitrogen-vacancy centers in diamond, Nano Lett. **18**, 4046 (2018).

[47] N. B. Manson, J. P. Harrison, and M. J. Sellars, Nitrogen-vacancy center in diamond: Model of the electronic structure and associated dynamics, Phys. Rev. B **74**, 104303 (2006).

[48] S. Sangtawesin, B. L. Dwyer, S. Srinivasan, J. J. Allred, L. V. H. Rodgers, K. De Greve, A. Stacey, N. Dontschuk, K. M. O'Donnell, D. Hu, D. A. Evans, C. Jaye, D. A. Fischer, M. L. Markham, D. J. Twitchen, H. Park, M. D. Lukin, and N. P. de Leon, Origins of Diamond Surface Noise Probed by Correlating Single-Spin Measurements with Surface Spectroscopy, Phys. Rev. X **9**, 031052 (2019).

[49] J.-P. Tetienne, R. W. De Gille, D. A. Broadway, T. Teraji, S. E. Lillie, J. M. McCoey, N. Dontschuk, L. T. Hall, A. Stacey, D. A. Simpson, and L. C. L. Hollenberg, Spin properties of

dense near-surface ensembles of nitrogen-vacancy centers in diamond, Phys. Rev. B **97**, 085402 (2018).

[50] E. Ravera, C. Luchinat, and G. Parigi, Basic facts and perspectives of Overhauser DNP NMR, J. Magn. Reson. **264**, 78 (2016).

[51] Q. Chen, I. Schwarz, F. Jelezko, A. Retzker, and M. B. Plenio, Resonance-inclined optical nuclear spin polarization of liquids in diamond structures, Phys. Rev. B **93**, 060408(R) (2016).

[52] J. H. Ardenkjær-Larsen, B. Fridlund, A. Gram, G. Hansson, L. Hansson, M. H. Lerche, R. Servin, M. Thaning, and K. Golman, Increase in signal-to-noise ratio of >10,000 times in liquid-state NMR, Proc. Natl. Acad. Sci. **100**, 10158 (2003).

[53] C.-G. Joo, K.-N. Hu, J. A. Bryant, and R. G. Griffin, In situ temperature jump high-frequency dynamic nuclear polarization experiments: Enhanced sensitivity in liquid-state NMR spectroscopy, J. Am. Chem. Soc. **128**, 9428 (2006).

[54] K. Kouřil, H. Kourilova, S. Bartram, M. Levitt, and B. Meier, Scalable dissolution-dynamic nuclear polarization with rapid transfer of a polarized solid, Nat. Commun. **10**, 1733 (2019).

[55] L. M. Pham, N. Bar-Gill, D. Le Sage, C. Belthangady, A. Stacey, M. Markham, D. J. Twitchen, M. D. Lukin, and R. L. Walsworth, Enhanced metrology using preferential orientation of nitrogen-vacancy centers in diamond, Phys. Rev. B **86**, 121202(R) (2012).

[56] F. F. de Oliveira, D. Antonov, Y. Wang, P. Neumann, S. A. Momenzadeh, T. Häußermann, A. Pasquarelli, A. Denisenko, and J. Wrachtrup, Tailoring spin defects in diamond, Nat. Commun. **8**, 15409 (2017).

[57] E. D. Herbschleb, H. Kato, Y. Maruyama, T. Danjo, T. Makino, S. Yamasaki, I. Ohki, K. Hayashi, H. Morishita, M. Fujiwara, and N. Mizuochi, Ultra-long coherence times amongst room-temperature solid-state spins, Nat. Commun. **10**, 3766 (2019).

[58] T. Lühmann, R. John, R. Wunderlich, J. Meijer, and S. Pezzagna, Coulomb-driven single defect engineering for scalable qubits and spin sensors in diamond, Nat. Commun. **10**, 4956 (2019).

[59] G. Kucsko, S. Choi, J. Choi, P. C. Maurer, H. Zhou, R. Landig, H. Sumiya, S. Onoda, J. Isoya, F. Jelezko, E. Demler, N. Y. Yao, and M. D. Lukin, Critical Thermalization of a Disordered Dipolar Spin System in Diamond, Phys. Rev. Lett. **121**, 023601 (2018).

[60] E. Bauch, S. Singh, J. Lee, C. A. Hart, J. M. Schloss, M. J. Turner, J. F. Barry, L. M. Pham, N. Bar-Gill, S. F. Yelin, and R. L. Walsworth, Decoherence of ensembles of nitrogen-vacancy centers in diamond, Phys. Rev. B **102**, 134210 (2020).

[61] G. de Lange, Z. H. Wang, D. Ristè, V. V. Dobrovitski, and R. Hanson, Universal dynamical decoupling of a single solid-state spin from a spin bath., Science **330**, 60 (2010).

[62] M. S. Grinolds, M. Warner, K. De Greve, Y. Dovzhenko, L. Thiel, R. L. Walsworth, S. Hong, P. Maletinsky, and A. Yacoby, Subnanometre resolution in three-dimensional magnetic resonance imaging of individual dark spins., Nat. Nanotechnol. **9**, 279 (2014).

[63] T. Rosskopf, A. Dussaux, K. Ohashi, M. Loretz, R. Schirhagl, H. Watanabe, S. Shikata, K. M. Itoh, and C. L. Degen, Investigation of Surface Magnetic Noise by Shallow Spins in Diamond, Phys. Rev. Lett. **112**, 147602 (2014).

[64] B. A. Myers, A. Das, M. C. Dartiailh, K. Ohno, D. D. Awschalom, and A. C. Bleszynski Jayich, Probing Surface Noise with Depth-Calibrated Spins in Diamond, Phys. Rev. Lett. **113**, 027602 (2014).

[65] Y. Romach, C. Müller, T. Unden, L. J. Rogers, T. Isoda, K. M. Itoh, M. Markham, A. Stacey, J. Meijer, S. Pezzagna, B. Naydenov, L. P. McGuinness, N. Bar-Gill, and F. Jelezko, Spectroscopy of Surface-Induced Noise Using Shallow Spins in Diamond, Phys. Rev. Lett. **114**, 017601 (2015).

[66] S. J. DeVience, L. M. Pham, I. Lovchinsky, A. O. Sushkov, N. Bar-Gill, C. Belthangady, F. Casola, M. Corbett, H. Zhang, M. Lukin, H. Park, A. Yacoby, and R. L. Walsworth, Nanoscale NMR spectroscopy and imaging of multiple nuclear species, Nat. Nanotechnol. **10**, 129 (2014).

[67] T. Staudacher, N. Raatz, S. Pezzagna, J. Meijer, F. Reinhard, C. A. Meriles, and J. Wrachtrup, Probing molecular dynamics at the nanoscale via an individual paramagnetic centre, Nat. Commun. **6**, 8527 (2015).

[68] H. Clevenson, M. E. Trusheim, C. Teale, T. Schröder, D. Braje, and D. Englund, Broadband magnetometry and temperature sensing with a light-trapping diamond waveguide, Nat. Phys. **11**, 393 (2015).

[69] A. Ajoy, X. Lv, E. Druga, K. Liu, B. Safvati, A. Morabe, M. Fenton, R. Nazaryan, S. Patel, T. F. Sjolander, J. A. Reimer, D. Sakellariou, C. A. Meriles, and A. Pines, Wide dynamic range magnetic field cycler: Harnessing quantum control at low and high fields, Rev. Sci. Instrum. **90**, 013112 (2019).

[70] J.-P. Tetienne, L. Rondin, P. Spinicelli, M. Chipaux, T. Debuisschert, J.-F. Roch, and V. Jacques, Magnetic-field-dependent photodynamics of single NV defects in diamond: An application to qualitative all-optical magnetic imaging, New J. Phys. **14**, 103033 (2012).

[71] L. M. Pham, S. J. DeVience, F. Casola, I. Lovchinsky, A. O. Sushkov, E. Bersin, J. Lee, E. Urbach, P. Cappellaro, H. Park, A. Yacoby, M. Lukin, and R. L. Walsworth, NMR technique for determining the depth of shallow nitrogen-vacancy centers in diamond, Phys. Rev. B **93**, 045425 (2016).

[72] D. B. Bucher, D. R. Glenn, H. Park, M. D. Lukin, and R. L. Walsworth, Hyperpolarization-Enhanced NMR Spectroscopy with Femtomole Sensitivity Using Quantum Defects in Diamond, Phys. Rev. X **10**, 021053 (2020).

[73] P. Kehayias, A. Jarmola, N. Mosavian, I. Fescenko, F. M. Benito, A. Laraoui, J. Smits, L. Bougas, D. Budker, A. Neumann, S. R. Brueck, and V. M. Acosta, Solution nuclear magnetic resonance spectroscopy on a nanostructured diamond chip, Nat. Commun. **8**, 188 (2017).

[74] I. Lovchinsky, A. O. Sushkov, E. Urbach, N. P. de Leon, S. Choi, K. De Greve, R. Evans, R. Gertner, E. Bersin, C. Müller, L. McGuinness, F. Jelezko, R. L. Walsworth, H. Park, and M. D. Lukin, Nuclear magnetic resonance detection and spectroscopy of single proteins using quantum logic, Science **351**, 836 (2016).

[75] N. Aslam, M. Pfender, P. Neumann, R. Reuter, A. Zappe, F. De Oliveira, A. Denisenko, H. Sumiya, S. Onoda, J. Isoya, and J. Wrachtrup, Nanoscale nuclear magnetic resonance with chemical resolution, Science **357**, 67 (2017).

[76] F. Ziem, M. Garsi, H. Fedder, and J. Wrachtrup, Quantitative nanoscale MRI with a wide field of view, Sci. Rep. **9**, 12166 (2019).

[77] I. Lovchinsky, J. D. Sanchez-Yamagishi, E. K. Urbach, S. Choi, S. Fang, T. I. Andersen, K. Watanabe, T. Taniguchi, A. Bylinskii, E. Kaxiras, P. Kim, H. Park, and M. D.

Lukin, Magnetic resonance spectroscopy of an atomically thin material using a single-spin qubit, Science **355**, 503 (2017).

[78] A. Laraoui, F. Dolde, C. Burk, F. Reinhard, J. Wrachtrup, and C. A. Meriles, High-resolution correlation spectroscopy of 13C spins near a nitrogen-vacancy centre in diamond, Nat. Commun. **4**, 1651 (2013).

[79] G. de Lange, D. Ristè, V. V. Dobrovitski, and R. Hanson, Single-Spin Magnetometry with Multipulse Sensing Sequences, Phys. Rev. Lett. **106**, 080802 (2011).

[80] J. F. Barry, J. M. Schloss, E. Bauch, M. J. Turner, C. A. Hart, L. M. Pham, and R. L. Walsworth, Sensitivity optimization for NV-diamond magnetometry, Rev. Mod. Phys. **92**, 015004 (2020).

[81] H. Ishiwata, H. C. Watanabe, S. Hanashima, T. Iwasaki, and M. Hatano, Label-free phase change detection of lipid bilayers using nanoscale diamond magnetometry, arXiv:2007.13085.

[82] D. A. Hopper, H. J. Shulevitz, and L. C. Bassett, Spin readout techniques of the nitrogen-vacancy center in diamond, Micromachines **9**, 437 (2018).

[83] P. R. Zangara, J. Henshaw, D. Pagliero, A. Ajoy, J. A. Reimer, A. Pines, and C. A. Meriles, Two-electron-spin ratchets as a platform for microwave-free dynamic nuclear polarization of arbitrary material targets, Nano Lett. **19**, 2389 (2019).